Quantitative Susceptibility Mapping of the Human Brainstem with 3T and 7T Magnetic Resonance Imaging

Diplomarbeit

zur Erlangung des akademischen Grades

Diplom-Ingenieur

im Rahmen des Studiums

Biomedical Engineering

ausgeführt an der

Fakultät für Physik der Technischen Universität Wien

unter Anleitung von

Em.Univ.Prof. Dipl.-Ing. Dr.techn. Gerald Badurek

in Zusammenarbeit mit

Assoc.Prof. Dr. Simon Robinson, MSc, BSc

an der

Universitätsklinik für Radiologie und Nuklearmedizin der Medizinischen Universität Wien

eingereicht von

Charles Joseph Guthrie

Matrikelnummer 11741620

_____   _____
(Unterschrift Verfasser)   (Unterschrift Betreuung)

Wien, 13. Mai 2020

TU WIEN

TECHNISCHE UNIVERSITÄT WIEN

Vienna University of Technology

Quantitative Susceptibility Mapping of the Human Brainstem with 3T and 7T Magnetic Resonance Imaging

Master's Thesis

submitted in fulfillment of requirements for the degree of

Master of Science

in

Biomedical Engineering

completed at the

Faculty for Physics of the Technical University of Vienna

under the supervision of

Em.Univ.Prof. Dipl.-Ing. Dr.techn. Gerald Badurek

in cooperation with

Assoc.Prof. Dr. Simon Robinson, MSc, BSc

at the

Department of Biomedical Imaging and Image-guided Therapy of the Medical

University of Vienna

submitted by

Charles Joseph Guthrie

Matriculation number 11741620

_____   _____
(Author Signature)   (Advisor Signature)

Vienna, 13. Mai 2020

Erklärung zur Verfassung der Arbeit

Charles Joseph Guthrie
Mechelgasse 8/1, 1030, Wien, Österreich

Hiermit erkläre ich, dass ich diese Arbeit selbstständig verfasst habe, dass ich die verwendeten Quellen und Hilfsmittel vollständig angegeben habe und dass ich die Stellen der Arbeit – einschließlich Tabellen, Karten und Abbildungen –, auf anderen Werken oder dem Internet im Wortlaut oder dem Sinn nach entnommen sind, auf jeden Fall unter Angabe der Quelle als Entlehnung kenntlich gemacht habe.

_____   _____
(Ort, Datum)   (Unterschrift Verfasser)

Acknowledgements

My deepest thanks go to several people who played instrumental roles throughout the course of my project work and master thesis at the High Field MR Center. First, to Simon Robinson, my local supervisor at the Medical University of Vienna. He introduced me to MR research while providing a steady hand and patient feedback throughout the course of my work. I would also like to thank Karin Poljanc, professor at the Technical University of Vienna, for connecting me with the MR Center and for organizing my thesis activity at the TU. Additionally, I would like to thank Gerald Badurek, professor emeritus at the Technical University of Vienna, for advising my thesis.

My heartfelt appreciation also goes to Beáta Bachratá, Pedro Cardoso, Korbinian Eckstein, David Bancelin, and Andreas Ehrmann for their technical support and friendship throughout the project. They all made for a wonderful group to work with day in and day out during my time at the institute.

Lastly, I would like to acknowledge the delicious food at the Mensa at the Vienna General Hospital for daily giving me the physical and mental fuel to perform my research.

List of Abbreviations

ALS	Amyotrophic Lateral Sclerosis
ASPIRE	A Simple Phase Image Reconstruction for Multi-echo Data
BET	Brain Extraction Tool
CN	Caudate Nuclei
CNR	Contrast-to-Noise Ratio
CSF	Cerebrospinal Fluid
CWM	Cerebral White Matter
DBS	Deep Brain Stimulation
DICOM	Digital Imaging and Communications in Medicine
EPI	Echo Planar Imaging
FA	Flip Angle
FAST-STEM	Functional and Structural Identification of Targets in the Brainstem
FID	Free Induction Decay
fMRI	functional MRI
FOV	Field of View
fQSM	functional QSM
FSL	FMRIB Software Library
FT	Fourier Transform
GM	Gray Matter
GP	Globus Pallidus
GRAPPA	Generalized Autocalibrating Partially Parallel Acquisitions
GRE	Gradient-recalled Echo
IC	Internal Capsule
iHARPERELLA	integrated Harmonic Background Phase Removal using the Laplacian Operator
iLSQR	iterative Least Squares
LBV	Laplacian Boundary Value
MEDI	Morphology-enabled Dipole Inversion

MRI	Magnetic Resonance Imaging
MS	Multiple Sclerosis
NMR	Nuclear Magnetic Resonance
PD	Parkinson's Disease
PDF	Projection onto Dipole Fields
PI	Parallel Imaging
PU	Putamen
QSM	Quantitative Susceptibility Mapping
rBW	receiver Bandwidth
RF	Radiofrequency
RN	Red Nuclei
ROI	Region of Interest
SEGUE	Speedy Region-growing Algorithm for Unwrapping Estimated Phase
SHARP	Sophisticated Harmonic Artifact Reduction for Phase Data
SN	Substantia Nigra
SNpc	Substantia Nigra pars compacta
SNR	Signal-to-Noise Ratio
STAR-QSM	Streaking Artifact Reduction in QSM
STI	Susceptibility Tensor Imaging
STN	Subthalamic Nucleus
SWI	Susceptibility Weighted Imaging
TBI	Traumatic Brain Injury
TE	Echo Time
TPU	Temporal Phase Unwrapping
TR	Repetition Time
UMPIRE	Unwrapping Multi-echo Phase Images with Irregular Echo Spacings
VOI	Volume of Interest
VSHARP	Variable Kernel SHARP
WM	White Matter

Table of Contents

1 Abstract

Quantitative susceptibility mapping (QSM) is a method in magnetic resonance imaging (MRI) that depicts the spatial distribution of local magnetic susceptibilities of tissue. Magnetic susceptibility is an intrinsic, material-specific measure of the extent to which a material becomes magnetized in an external magnetic field. The phase of the inherently complex MR signal is used to generate QSM images, known as susceptibility maps.

Gradient-recalled Echo (GRE) sequences are typically used for QSM because they contain T_2*-weighting and their phase maps reflect the sample magnetization, and thus its magnetic susceptibility. Echo Planar Imaging (EPI) acquires an entire slice containing T_2*-weighting in 50-100 milliseconds. Because EPI phase maps also reflect sample magnetization, they can be used to generate susceptibility maps. Though EPI suffers from geometric distortions and signal dropout, drawbacks that do not afflict GRE, it is significantly faster.

Constructing a susceptibility map requires coil channel combination of phase data, phase unwrapping, brain masking, background field removal, and solving the field-to-source inverse problem of the dipole kernel. QSM provides contrast between grey matter (GM), white matter (WM), myelin, and iron. This enables many brain structures, including those in the brainstem, to be visualized with more clarity than is possible in T_1- and T_2*-weighted images.

QSM presents an exciting opportunity to localize brainstem nuclei owing to their relatively high susceptibilities. Localizing brainstem nuclei could aid patient-specific neurosurgical planning, specifically the implantation of electrodes used for deep brain stimulation (DBS), a surgical intervention used to alleviate symptoms in Parkinson's Disease, a common neurodegenerative disorder. MR imaging of the brainstem is challenging because brainstem nuclei are small and in close proximity to each other, GM and WM contrast is diminished by complex interwoven structures, and physiological noise is caused by cardiac and respiratory pulse waves.

The aim of this thesis was to develop QSM pipelines to generate the best possible susceptibility maps derived from EPI and GRE sequences, at both high and ultra-high field, as measured by their ability to quantify local tissue susceptibility and localize subcortical brainstem nuclei. Additionally, this study explored strategies to overcome both EPI's inherent drawbacks and challenges posed by the brainstem to yield susceptibility maps of sufficient quality to be a standalone option for rapid QSM imaging of brainstem nuclei.

It was shown that Laplacian-based phase unwrapping, a combination of BET and SPM brain masking, VSHARP background field removal, and STAR-QSM dipole inversion produced the highest quality susceptibility maps for both EPI and GRE images.

2-D EPI-QSM images yielded sufficient contrast-to-noise ratios to localize all six subcortical and brainstem nuclei at both high and ultra-high field. Susceptibilities of brainstem nuclei more closely matched literature values at high field. Further, EPI-QSM images benefitted from time-averaging several measurement repeats and GRE-QSM images benefitted from echo-averaging multi-echo acquisitions. These approaches made it possible to measure susceptibilities in deep gray matter structures in the inferior brain in seconds, providing the methodological basis for identification of brainstem nuclei to aid surgical implantations of DBS electrodes based on rapid QSM.

2 Kurzfassung

Quantitative Susceptibility Mapping (QSM) ist ein Verfahren der Magnetresonanztomographie, das aufgrund von lokalen Abweichungen des Magnetfeldes magnetische Suszeptibilitäten des Gewebes darstellen kann. Die magnetische Suszeptibilität ist eine intrinsische, materialspezifische Eigenschaft, die bemisst, wie stark ein Material in einem externen Magnetfeld magnetisiert wird. Die Phaseninformation des komplexen MR-Signals wird zur Erzeugung der QSM-Bilder, sogenannter Suszeptibilitätskarten, verwendet.

Gradienten-Echo (GRE)-Bilder werden typischerweise für QSM verwendet, da sie eine T_2*-Gewichtung beinhalten und ihre Phasenkarten die Magnetisierung der Probe und damit ihre magnetische Suszeptibilität widerspiegeln. Echo-Planar-Imaging (EPI) erfasst eine ganze Schicht mit T_2*-Gewichtung in 50-100 Millisekunden. Da EPI-Phasenkarten auch die Probenmagnetisierung widerspiegeln, können sie zur Erzeugung von Suszeptibilitätskarten verwendet werden. Obwohl EPI unter geometrischen Verzerrungen und Signalausfällen leidet, Nachteile, die GRE nicht betreffen, ist es wesentlich schneller.

Für das Erstellen einer Suszeptibilitätskartierung sind die Kombination der Spulenkanäle, die Phasensprungkorrektur, die Maskierung des Gehirns, das Entfernen der Hintergrundvariation, und das Lösen des inversen Feld-zu-Quelle-Problems des Dipolfelds erforderlich. QSM ermöglicht Kontraste zwischen grauer Substanz (GM), weißer Substanz (WM), Eisen und Myelin. Durch diese Kontraste lassen sich viele Hirnstrukturen, einschließlich Strukturen, die sich im Hirnstamm befinden, besser visualisieren als in T_1- und T_2*-gewichteten Bildern.

QSM bietet eine vielversprechende Möglichkeit, Hirnstammkerne zu lokalisieren, aufgrund ihrer relativ hohen Suszeptibilitäten. Die Lokalisierung von Hirnstammkernen könnte die patientenspezifische neurochirurgische Planung unterstützen, insbesondere die Implantation von Elektroden zur tiefen Hirnstimulation, einem chirurgischen Eingriff zur Linderung von Symptomen bei der Parkinson-Krankheit, einer häufigen neurodegenerativen Erkrankung. Die MR-Bildgebung des Hirnstamms stellt eine Herausforderung dar, da die Hirnstammkerne klein sind und nahe beieinander liegen, der GM- und WM-Kontrast durch komplexe verflochtene Strukturen vermindert ist und physiologische Geräusche durch Herz- und Atempulswellen verursacht werden.

Das Ziel dieser Masterarbeit war es, eine QSM-Verfahrensweise zu entwickeln, um die bestmöglichen Suszeptibilitätskarten zu erzeugen, die aus EPI- und GRE-Sequenzen, sowohl im hohen als auch im ultrahohen Feld, abgeleitet sind. Diese wurden nach ihrer Fähigkeit, die lokale Gewebe-Suszeptibilität zu quantifizieren und subkortikale Hirnstammkerne zu lokalisieren, bewertet. Zusätzlich untersuchte diese Studie Strategien zur Überwindung sowohl der inhärenten Nachteile von EPI als auch der Herausforderungen, die der Hirnstamm mit sich bringt, um Suszeptibilitätskarten von ausreichender Qualität zu erhalten, welche eine eigenständige Option für die schnelle QSM-Bildgebung von Hirnstammkernen darstellen.

Es wurde gezeigt, dass die Laplace-Operator-basierte Phasensprungkorrektur, eine Kombination aus BET- und SPM-Gehirnmaskierung, VSHARP-Hintergrundfeldentfernung und STAR-QSM-Dipolinversion sowohl für EPI- als auch für GRE-Bilder die höchste Qualität der Suszeptibilitätskarten ergab. 2-D-EPI-QSM-Bilder ergaben ein ausreichendes Kontrast-Rausch-Verhältnis, um alle sechs analysierten subkortikalen und Hirnstammkerne sowohl im Hoch- als auch im Ultrahochfeld zu lokalisieren. Die Suszeptibilitäten der Hirnstammkerne stimmten im Hochfeld genauer mit den Literaturwerten überein. Darüber hinaus profitierten EPI-QSM-Bilder von der zeitlichen Mittelung mehrerer Messwiederholungen und GRE-QSM-Bilder von echomittelnden Multi-Echo-Aufnahmen.

3 Introduction

3.1 Motivation

Located in the posterior region of the brain, the brainstem is an important hub for nerve pathways between the brain and the rest of the body. Along the ventral-dorsal axis, the brainstem is made up of the midbrain, the pons, and the medulla oblongata. Ventral to the midbrain is the thalamus, along with other subcortical structures. Dorsal to the medulla is the spinal cord. Ten out of the twelve cranial nerves originate in the brainstem. Additionally, it plays a role in cardiovascular and respiratory control, as well as regulation of pain, awareness, and consciousness.

Parkinson's disease (PD) can involve degradation of neurons in the substantia nigra pars compacta (SNpc), a structure in the midbrain (1). One therapy for PD is deep brain stimulation (DBS) (2). DBS is a surgical intervention to implant electrodes that periodically stimulate the nerve tissue into structures such as the globus pallidus (GP) and subthalamic nucleus (STN) (3).

A deciding factor in the efficacy of DBS is the placement of the electrodes. Currently, electrodes are placed according to intra-operative feedback from the conscious patient and standard brain atlases, however, location of brainstem structures may vary widely from patient to patient (4). Localizing subcortical and brainstem structures for individual patients via magnetic resonance imaging (MRI) may improve accurate implantation of DBS electrodes (5). An MR method called quantitative susceptibility mapping (QSM) (6–8) can produce images well suited to identifying subcortical and brainstem structures.

MR signal is inherently complex and can be split into phase and magnitude components. Conventionally, only the magnitude component is used to generate images, but QSM is part of a growing field based on processing of the phase component. QSM utilizes perturbations in the local magnetic field induced by the magnetic susceptibilities of brain tissue to produce an image. Thus, differences in magnetic susceptibility between tissues produces contrast in QSM. This is particularly useful in visualizing gray matter and white matter contrast (9), intracranial calcifications (10), cerebral lesions (11), and iron concentration (12).

Subcortical and brainstem nuclei can be delineated from surrounding tissue based on their elevated iron compositions (13) because susceptibility maps demonstrate high linear correlation with ferric iron concentration (14,15). QSM has been shown to allow better delineation of deep brain structures in adjacent tissues than T_2*-weighted images (16). It can be useful in identifying indicators of PD (17) as well as other neurodegenerative disorders such as multiple sclerosis (MS) (18) because of the central role that brain iron levels play in the complicated pathophysiology of neurodegenerative disease (19).

QSM has often been carried out on images from 3-dimensional gradient recalled echo (GRE) sequences because their phase maps reflect the tissue magnetization and thus its inherent susceptibility (20). However, 3-D GRE sequence must make compromises between resolution and scan time. A 1 mm isotropic whole head scan requires about 10 minutes of acquisition time (21).

An alternative sequence that has a markedly faster acquisition time is the echo planar imaging (EPI) sequence (22). A whole-head volume can be acquired in a few seconds, a crucial advantage in clinical practice. EPI is also sensitive to local field inhomogeneities necessary for

producing susceptibility maps. EPI has been shown to produce similar susceptibility values as GRE images (23).

There are several drawbacks inherent in EPI that present challenges for EPI-based QSM, particularly at ultra-high field and in the brainstem. EPI images contain geometric distortions arising from the long readout period of the sequence, where off-resonance phase errors accumulate in the phase-encoding direction (24). Geometric distortions arise from static magnetic field inhomogeneities. These are especially strong near tissue-air junctions in the brain, such as those posterior to the paranasal sinuses (25). EPI sequences, due to their longer readout bandwidth (on the order of 1000+ Hz/pixel) suffer from lower signal-to-noise ratio (SNR) than their GRE counterparts. EPI images suffer additionally from limits on resolution caused by high gradient power demands on the hardware and signal dropout, especially at ultra-high field.

If QSM methods based on fast-acquisition 2-D EPI images can be established to produce sufficiently reliable susceptibility maps, they present a promising opportunity to rapidly acquire images relevant to localizing subcortical and brainstem structures. This step overcomes long acquisition time, a key drawback to QSM's viability as a clinically relevant MR technique.

3.2 Aim

The aim of this thesis was to develop QSM pipelines to generate the best possible susceptibility maps derived from 2-D EPI, 2-D GRE, and 3-D GRE sequences, at both high and ultra-high field, as measured by their ability to quantify local tissue susceptibility and localize subcortical brainstem nuclei. Additionally, this study explored 2-D EPI strategies with the goal of overcoming EPI's inherent drawbacks and challenges posed by the brainstem to yield susceptibility maps of sufficient quality to be a standalone option for rapid QSM imaging of brainstem nuclei.

4   Theory

4.1   Principles of Magnetic Resonance Imaging

MRI is based on the principle nuclear magnetic resonance (NMR). It makes use of strong magnetic fields, magnetic field gradients, and excitation radio waves to create a signal that reflects proton density and tissue relaxation times. MRI is widely used in diagnostic medicine due its noninvasiveness and lack of ionizing radiation that exists in other common medical imaging modalities such as x-rays and CT scans. Owing to the range of excitation sequences in MRI, it is a flexible modality that can produce images for many anatomical regions and many tissue types (26)[1].

4.1.1   Magnetic Spin & Magnetization

NMR signal is based on the nuclear spin of atoms placed in a strong magnetic field. Hydrogen atoms in water molecules are the primary atoms utilized in MRI. In the classical model, the proton's interaction with an external magnetic field produces a precession of its nuclear spin about the field direction, B_0. Precession is the circular motion of a spinning body around a fixed axis. In this case, the fixed axis is B_0.

The magnetic dipole moment, μ, is a vector of the strength and orientation of a magnet that produces a magnetic field, represented by a magnetic dipole. It relates the amount of torque acting on a magnetic object in the presence of an external magnetic field. It depends on both the field strength and the orientation of the proton relative to the field. The direction of μ indicates the spin axis of the proton.

In the absence of thermal energy, the proton would tend to align itself along the magnetic field axis. However, thermal energy is millions of times larger than the energy of nuclear spin of a proton's alignment with the externally applied magnetic fields used in MRI. Therefore, the proton will precess around the B_0 axis, in a path depicted in Figure 1.
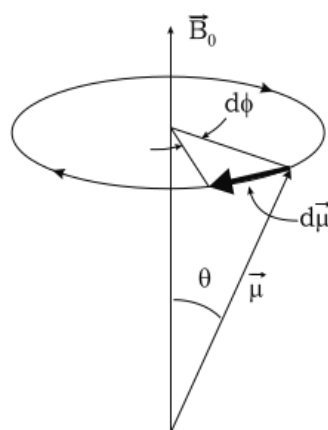

Figure 1: Precession of a proton around the magnetic field axis in the presence of thermal energy. Adapted from (26).

---

[1] Unless otherwise noted, all equations and figures until Section 4.1.4 are derived from Brown et al. Ch 1.

The angular frequency of the precession linearly depends on the strength of the external magnetic field. The ratio of the two is a constant, called the gyromagnetic ratio, γ, defined as

$$\gamma = \frac{\omega_0}{B_0} \tag{4.1}$$

where ω_0 is the precession angular frequency, also known as the Larmor frequency. In water, the gyromagnetic ratio is roughly 2.8×10^8 radians per second per tesla, or 42.6 MHz per tesla.

A single proton has two possible quantum spin states: parallel or antiparallel to the magnetic field. The antiparallel spin state's quantum energy difference to the parallel spin state is equal to the Larmor precession frequency and is much smaller than the thermal energy of the system. Therefore, the ratio of excess spins in the lower energy parallel state compared to the higher energy antiparallel state, known as the spin excess, is defined by a Boltzmann probability distribution and is relatively small at room temperature, on the order of 10^{-6}. The spin excess, though small, enables the signal arising from NMR, because of the spin density, or the number of protons per unit volume, which is on the order of Avogadro numbers for even small regions of tissue.

Bringing together the spin excess, spin density, and proton magnetic moment results in the longitudinal equilibrium magnetization, M_0, defined as

$$M_0 = \frac{\rho_0 \gamma^2 \hbar^2}{4kT} B_0 \tag{4.2}$$

where ρ_0 is the spin density, $\hbar$ is the reduced Planck's constant, k is the Boltzmann's constant, and T is temperature. By this relation, the bulk magnetization of a system is proportional to the longitudinal equilibrium magnetization.

4.1.2   Radiofrequency Excitation

Because it is in an equilibrium state, bulk magnetization arising from the spin excess does not create a meaningful NMR signal alone. The system must be energized to tip the magnetic moment vector, μ, and thus the magnetization, M_0, away from the B_0 direction. This excitation causes precession of the magnetic moment around the external magnetic field to rotate out of alignment with B_0, and energizes the system with energy that will create a signal during its release.

A radiofrequency (RF) pulse is applied to the target to excite it away from its alignment with B_0 and into the transverse direction. The RF pulse must be generated at the Larmor frequency in order to achieve resonance and coherently excite the tissue into the transverse plane. If the longitudinal direction is considered to be the z direction, then the RF-excited tissue will precess in the x-y plane. If the RF pulse rotates the net magnetization vector M until it is orthogonal to B_0, then M has magnitude equal to M_0 and is known as the transverse magnetization, while the excitation pulse is known as a 90° or $\pi/2$ pulse.

The RF pulse synchronizes the precession phases of protons at the Larmor frequency of the excitation pulse, which is the resonant frequency of the system. A transmit coil produces the RF excitation frequency.

4.1.3   Relaxation & Nuclear Magnetic Resonance

When the RF excitation pulse stops, the system leaves its excited state and returns to orientation along the z axis, towards thermal equilibrium. Transverse magnetization M_0 begins to precess

again in the x-y plane back towards the z axis. During this relaxation process, the magnetization is complex-valued, defined by

$$M(t) = M_x(t) + iM_y(t) = M_0 e^{-i\omega_0 t + i\varphi_0} \tag{4.3}$$

where M_0 is the initial magnitude of the precessing magnetization moment and φ_0 is the polar angle of this precession, the direction of the magnetization vector projected in the x-y plane.

The rotating magnetization resulting from relaxation of *M(t)* back towards B_0 causes a time-varying magnetic flux that induces an electrical current in a receive coil. This receive coil can be the same coil as the transmit coil, in which case it is known as the transceive coil. The voltage in the receive coil, the signal, is proportional to the precession angular frequency ω_0 and M_0. NMR signal depends on the gyromagnetic ratio, static magnetic field strength, spin density, and temperature according to

$$signal \propto \frac{\gamma^3 B_0 \rho_0}{T}. \tag{4.4}$$

Two forms of relaxation are in play in NMR: spin-lattice and spin-spin relaxation.

Spin-lattice relaxation, also known as T_1 or longitudinal relaxation, is the recovery of the nuclear spin magnetization back towards thermal equilibrium, that is, alignment along the z axis. M_z then varies with time according to

$$M_z(t) = M_{z,eq}(1 - e^{-\frac{t}{T_1}}) \tag{4.5}$$

where $M_{z,eq}$ is the magnetization vector at thermal equilibrium and T_1 is the time constant for spin-lattice relaxation. Lattice in this case refers to a field of neighboring atoms, where spin-lattice relaxation indicates that nuclear spin energy is exchanged with the lattice, or a given atom's surroundings in order for the system to return to equilibrium.

T_1 relaxation is dependent on the Larmor frequency, which in turn depends on the magnetic field strength. The T_1 relaxation time is a characteristic time constant, i.e. the time at which the system is restored to 63% of its equilibrium value. T_1 values will vary according to the tissue type, tissue environment, and field strength at which the tissue is imaged.

Spin-spin relaxation, or T_2 relaxation, is the decoherence of the transverse component of magnetization, M_{xy}. In contrast to M_z in T_1 relaxation, which increases in magnitude over time, M_{xy} decays to zero in T_2 relaxation, as the tissue is eventually completely dephased, according to

$$M_{xy}(t) = M_{xy}(0)e^{-\frac{t}{T_2}}. \tag{4.6}$$

Phase coherence created by the RF excitation pulse is lost via random variation and fluctuations in the magnetic field as well as direct interactions between spins that lead to different precession frequencies. When the phases of precession are completed disordered, the net transverse magnetization is zero and the tissue is completed dephased. The T_2 relaxation time is a characteristic time constant defined by the time at which M_{xy} loses 63% of its original magnitude. As opposed to T_1 relaxation, T_2 relaxation does not vary strongly according to field strength.

Macroscopic magnetization as a function of time and relaxation constants T_1 and T_2 can be elegantly described by the Bloch equation,

$$\frac{dM(t)}{dt} = \left(M(t) \times B(t)\right) + \frac{1}{T_1}(M_0 - M_z)\hat{z} - \frac{1}{T_2}M_{xy} \tag{4.7}$$

where *M(t)* is the time-varying total magnetization vector and *B(t)* is the magnetic field experienced by the protons. While *B(t)* would equal B_0 under circumstances without excitation, under time-varying magnetic fields, *B(t)* is defined in three dimensions as

$$B(t) = (B_x(t), B_y(t), B_0 + G_z(t))) \tag{4.8}$$

where *G_z(t)* is the gradient magnetic field. The trajectory of the net magnetization follows a narrowing spiral path as shown in Figure 2.
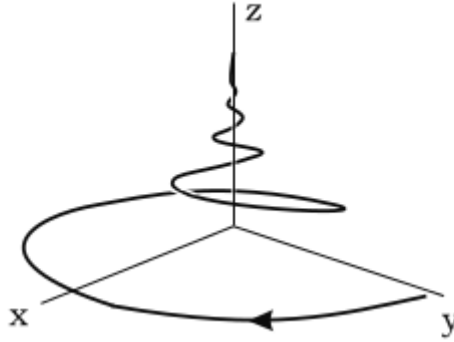

Figure 2: General trajectory of net magnetization during an NMR relaxation process, illustrating the characteristic spiral-shaped return to thermal equilibrium. From this process, an FID signal is produced. Adapted from (26).

The progression of magnetization over time described by the Bloch equation forms the foundation for applying the principle of nuclear magnetic resonance to magnetic resonance imaging.

The simplest form of excitation and relaxation described above, when the sample is energized until there is transverse magnetization and then is allowed to relax back to thermal equilibrium, is known as free induction decay (FID). FID signal is acquired as the magnetization reorients towards B_0 and as dephasing occurs. The signal recorded is a sine wave with frequency at the Larmor frequency, decaying exponentially according to both T_2 relaxation and local magnetic inhomogeneities, collectively referred to as T_2^* decay. Because local magnetic inhomogeneities will always exist to a certain extent in a system, T_2^* decay will always be shorter than its T_2 counterpart.

FID is a basic MR signal formed by a simple RF excitation pulse. More complicated excitation sequences incorporate different pulse patterns to produce different signals.

4.1.4   *From Nuclear Magnetic Resonance Signal to Imaging*

The goal of MRI is to determine the spatial distribution of tissues within a sample. The key bridge connecting the NMR *signal* to an MR *image* is the gyromagnetic ratio, that is, the relationship between magnetic field strength and Larmor frequency. In the presence of a spatially changing magnetic field, tissue produces a spatially changing frequency signal according to

$$w(x) = \gamma B(x) \tag{4.9}$$

where *x* indicates a position along a magnetic field gradient. If the magnetic field *B* at position *x* is known, and the frequency is tuned to a particular frequency, then a specific region's spectroscopic signal will correspond to a spatial location.

When the magnetic field gradient is linear in a particular direction, the phase of the tissue magnetization also varies linearly. Due to this linear relationship, the conversion from NMR signal space to image position space is carried out simply with a Fourier transform. The signal is effectively a Fourier transform of the spin density. The image is then reconstructed from an inverse Fourier transform.

The magnetic field gradient is produced by a second coil, the linear gradient coil, so the total magnetic field is in fact a summation of the large static magnetic B_0 and a smaller linearly varying field $B(x)$. To excite one region of tissue, the RF excitation pulse is finite and centered around the Larmor frequency of tissue, which can be calculated by

$$f = \frac{\gamma}{2\pi}\big(B_0 + B(x)\big). \tag{4.10}$$

The RF pulse width, δf, linearly corresponds to the spatial excitation width, or slice thickness δx. A volume is imaged in MRI by exciting one 2-D volume with a certain slice thickness at a time and then stacking successive 2-D volumes, or slices, next to each other to form a 3-D image set.

4.1.4.1 *Frequency Encoding of Spin Position*

Taking into account MR scanner hardware used in detection, and principles of signal detection based on Faraday's law of electromagnetic induction, the complex-valued signal as a function of sample magnetization is given by[2]

$$s(t) \propto \omega_0 \int d^3 r e^{-\frac{t}{T_2(r)}} M_\perp(\vec{r}, 0) B_\perp(\vec{r}) e^{i((\Omega - \omega_0)t + \varphi_0(\vec{r}) - \Theta_B(\vec{r}))} \tag{4.11}$$

where $s(t)$ is the complex signal, ω_0 is the Larmor frequency, $M_\perp$ is the magnitude of transverse magnetization, commonly in the z direction, $B_\perp$ is the transverse magnetic field, Ω is a reference signal frequency, φ_0 is the signal phase, and Θ_B is the receive field directional phase. When the transmitting- and receiving-RF coils are considered uniform and relaxation effects are ignored, and gain factors from the detection array are combined into a coefficient Λ, then the signal is

$$s(t) = \omega_0 \Lambda B_\perp \int d^3 r M_\perp(\vec{r}, 0) e^{i(\Omega t + \varphi(\vec{r}, t))}. \tag{4.12}$$

The accumulated phase, $\varphi(\vec{r}, t)$, is considered positive in the counterclockwise direction and comprises the imaginary part of the MR signal, with the relationship

$$\varphi(\vec{r}, t) = -\int_0^t dt' \omega(\vec{r}, t') \tag{4.13}$$

where t' is time over the course of signal acquisition. Recall that, from Equation 4.2, the equilibrium magnetization, M_0, can be expressed in terms of spin density, ρ_0, as

$$M_\perp(\vec{r}, 0) = M_0(\vec{r}) = \frac{\rho_0 \gamma^2 \hbar^2}{4kT} B_0 \tag{4.14}$$

when the gradient magnetic field has not been activated yet. The perpendicular magnetization, $M_\perp$, is equivalent to the equilibrium magnetization at exactly $t=0$ when the excitation pulse is

---

[2] Unless otherwise noted, all equations, figures, and theory until 4.1.5. are derived from Brown et al. Ch 9.

a perfect $\pi/2$ pulse. By combining the signal, Equation 4.12, with the transverse magnetization, Equation 4.14, the signal is three dimensions is

$$s(t) = \int d^3r \rho(\vec{r}) e^{i(\Omega t + \varphi(\vec{r},t))} \qquad (4.15)$$

where $\rho(\vec{r})$ is the effective spin density, defined as

$$\rho(\vec{r}) = \omega_0 \Lambda B_\perp M_0(\vec{r}) = \omega_0 \Lambda B_\perp \frac{\rho_0 \gamma^2 \hbar^2}{4kT} B_0. \qquad (4.16)$$

Signal is a linear integral of the volume's net spin density, as it varies with time. (Note that in a sequence in which more than one excitation and acquisition are taken consecutively, relaxation effects come into play and $\rho(\vec{r})$ becomes a function $\rho(\vec{r}, T_1, T_2)$).

Simplified to one dimension, signal could be expressed as

$$s(t) = \int dz \rho(z) e^{i(\Omega t + \varphi(z,t))} \qquad (4.17)$$

and effective spin density as

$$\rho(z) = \iint dx dy \rho(\vec{r}). \qquad (4.18)$$

The relationship between spin density and signal forms the basis of frequency encoding in MRI.

The Larmor frequency of a nuclear spin is linearly proportional to z as long as the magnetic field gradient, G_z, varies linearly as well, as

$$G_z = \frac{\partial B_z}{\partial z} \qquad (4.19)$$

with the total z component of the magnetic field defined by

$$B_z(z,t) = B_0 + zG_z(t). \qquad (4.20)$$

The spatial variation of spin frequency in the excited tissue is

$$\omega(z,t) = \omega_0 + \omega_G(z,t). \qquad (4.21)$$

where the difference in frequency resulting from G_z is

$$\omega_G(z,t) = \gamma z G(t) \qquad (4.22)$$

and is referred to as frequency encoding in the z direction. As the gradient field acts on the tissue over time, the accumulated phase due to the presence of an applied gradient is

$$\phi_G(\vec{r},t) = -\int_0^t dt' \omega_G(\vec{r},t') = -\gamma z \int_0^t dt' G(t'). \qquad (4.23)$$

Under the influence of G_z, the frequency-encoded nuclear spins provide a spatially localizable signal. In one dimension, this is described by

$$s(t) = \int dz \rho(z) e^{i\varphi_G(z,t)} \qquad (4.24)$$

which relates to the general one-dimensional signal equation, except that the phase is expressed only as a function of the gradient magnetic field without a reference signal frequency, Ω. When more gradients are applied to the field, 2-D or 3-D imaging can take place, with associated equations in 2-D or 3-D.

4.1.5 Spatial Frequency & K-Space

K-space is the 2-D or 3-D Fourier-transformed signal and is complex-valued. It is an array representing spatial frequencies of the MR image. The intensity of each point in *k*-space correlates to the relative contribution of that particular spatial frequency to the overall MR image.

The signal dependence on spatial frequency, *k*, is exactly a Fourier transform of ρ_0, yielding a computationally straightforward equation to map NMR signal in *k*-space. In terms of the spatial frequency, signal is

$$s(k) = \int dz \rho(z) e^{-i2\pi kz} \tag{4.25}$$

where the time dependence is contained within *k* as

$$k(t) = \gamma \int_0^t dt' G(t'). \tag{4.26}$$

If *G* is constant in time, *k(t)* can be simplified to

$$k(t) = \gamma G t. \tag{4.27}$$

K-space is made up of cells on a Cartesian grid, with axes that are typically labeled k_x and k_y. These axes correspond to spatial frequencies in the *x* and *y* directions. Due to the nature of the Fourier transform, each *k*-space coordinate (k_x, k_y) contributes its particular spatial frequency to all points in image space. Conversely, one point (*x*, *y*) in image space is the summation of contributions from every single point in *k*-space. A sample *k*-space and image-space space is shown in Figure 3.
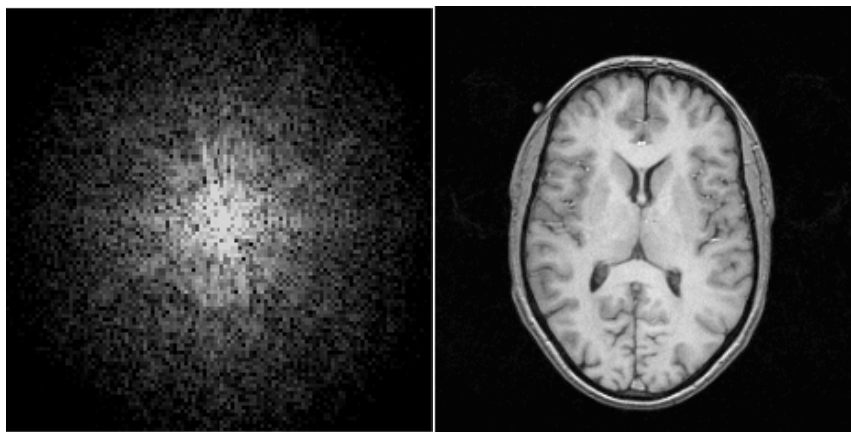
Figure 3: *K*-space (left) and image space (right) pair. Adapted from (27).

Points closer to the origin of *k*-space (the center of Figure 3), corresponding to lower spatial frequencies, contribute more heavily to general shapes, SNR, and contrast. Points closer to the edges of *k*-space (outer regions of Figure 3), corresponding to higher spatial frequencies, contribute more to fine detail and resolution. This phenomenon can be seen in Figure 4. The left-most column contains only the low spatial frequency *k*-space information, the center column contains only high spatial frequency information, and the right-most column contains the entire *k*-space.

Figure 4: Relationship between *k*-space and image space. An image reconstruction based only on points near the *k*-space origin (left column), reconstruction based only on points far away from the *k*-space origin (middle column), reconstruction based on the entire *k*-space (right column). Adapted from (28).

4.1.6 Gradient Echo Imaging

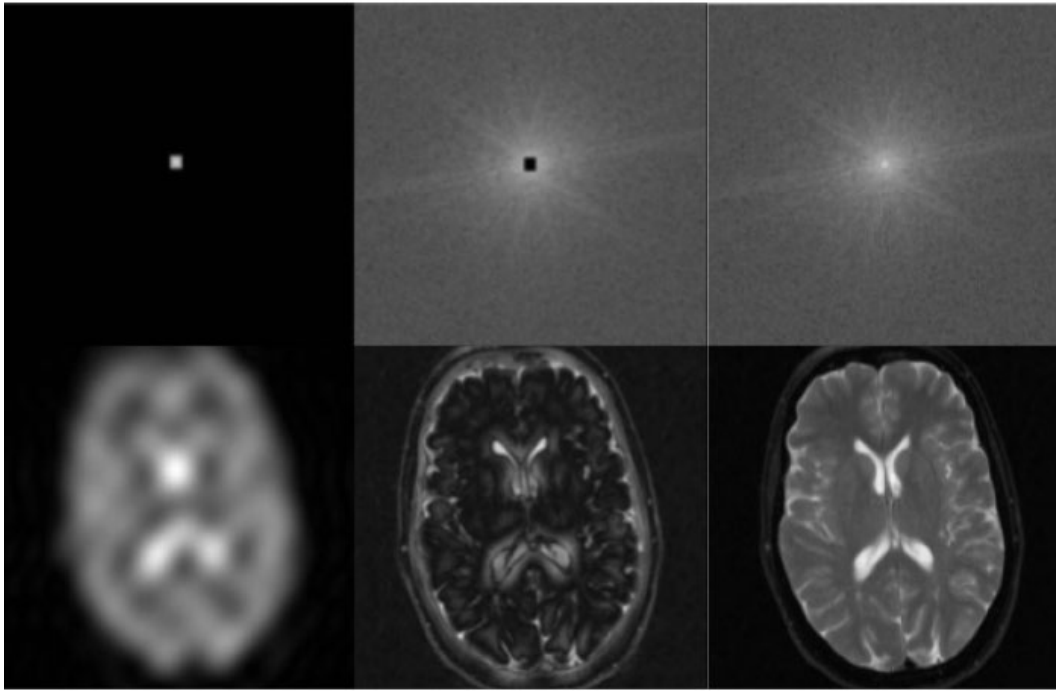The gradient-recalled echo sequence produces an image with T_2*-weighting. It is recalled that FID signal arises from an exponentially decaying sinusoidal signal with time constant T_2*, which reflects both T_2 relaxation and additional relaxation due to field inhomogeneities. A GRE sequence has features that decrease the sequence's repetition time, TR, and enable frequency encoding.

After the RF excitation pulse, a dephasing gradient accelerates the FID signal, which temporarily destroys the coherence of spins in a spatially dependent manner. A rephasing gradient is then applied, which has equal magnitude and opposite polarity of the dephasing gradient. When the phase change caused by the rephasing gradient is equal to the phase change caused by the dephasing gradient, determined by calculating the area under the curve of magnetic field gradient versus time, the dephasing caused by the readout gradient is reversed, except for the effects of field inhomogeneities. At this point, the signal is detected, and is referred to as the echo, or gradient echo. The difference between FID and GRE signal is illustrated in Figure 5.
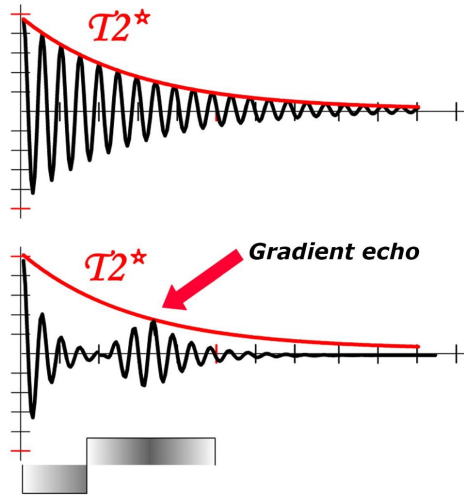
Figure 5: Signal versus time for FID (top) and GRE (bottom). The dephasing gradient, shown in the bottom left-hand corner, accelerates FID while the rephasing gradient creates an echo signal. Adapted from (29).

A pulse-timing diagram for a generic GRE sequence is shown in Figure 6. Peak signal occurs at the echo time, TE, which is the moment at which the phase distribution is optimally rephased to achieve maximum coherence. Signal is highest at exactly the TE, and signal magnitude is symmetrically distributed around the TE.
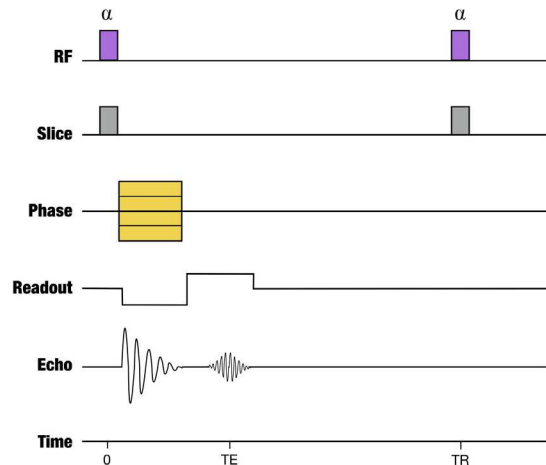
Figure 6: Pulse-timing diagram for a GRE sequence. Dephasing and rephasing gradients are apparent in the readout direction, causing maximum signal at the TE, with signal distributed symmetrically around TE. TR is much longer than TE to allow for demagnetization before the next excitation pulse. Adapted from (30).

Each gradient echo corresponds to signal acquisition along one line of k-space. The *k*-space trajectory begins at the origin, when the RF pulse is applied. The dephasing gradient then moves the *k*-space point to the beginning of one line, at the most negative value of k_x. As the rephasing gradient is applied, the *k*-space point moves horizontally along the line in *k*-space. The process is then repeated for all lines in 2-D *k*-space. As soon as one 2-D *k*-space matrix is sampled, the RF excitation frequency is adjusted to select for a different slice in the *z* direction, and the next 2-D *k*-space matrix is filled. Because one TR is required for traversal of each line in *k*-space, a GRE sequence typically takes several minutes to complete a whole-head scan.

GRE sequences are useful for QSM because they contain T_2* contrast and therefore contain information about local magnetic field inhomogeneities. GRE phase maps reflect the sample magnetization and thus its magnetic susceptibility.

4.1.6.1 Echo-Averaging in Gradient Echo Imaging

It is possible to have multiple echoes follow one excitation pulse, implemented in a method known as multi-echo GRE. A further pair of dephasing and rephasing gradients are added to the sequence after the first pair, and more pairs of gradient can continue to be added until T2* relaxation has diminished the signal entirely.

Multi-echo GRE is useful because ideal phase contrast is achieved when the TE is equal to the tissue's T_2* relaxation time (9). In vivo, T_2* relaxation times vary widely among tissue types, so single-echo GRE cannot provide ideal phase contrast within the entire brain. Multi-echo GRE gives more flexibility in finding the highest contrast based on magnetic susceptibility effects across the brain. By averaging susceptibility maps from each echo within a multi-echo GRE acquisition, Wu et al. showed that a tissue-optimized T_2* map was achievable (31). This concept could be extended to tissue-optimized susceptibility maps.

4.1.7 Echo Planar Imaging

EPI is a sequence that fills an entire 2-D *k*-space matrix from a single RF excitation pulse. It works by utilizing the same dephasing and rephasing frequency gradients as GRE to create echoes but includes many small phase gradients to move between lines in *k*-space, shown in Figure 7. The first large negative polarity phase gradient moves the signal point to the bottom edge of *k*-space. The small phase gradients then allow for a zig-zag movement through *k*-space, shown in the *k*-space image in Figure 7. Because EPI is based on the GRE sequence, it is also sensitive to T2* contrast.
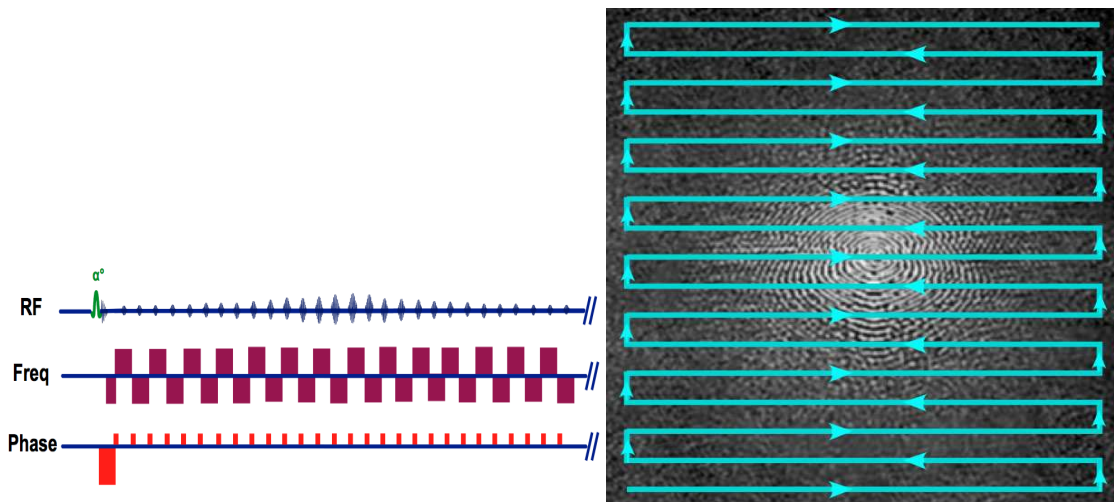
Figure 7: Frequency and phase encoding in an EPI sequence (left) and *k*-space traversal in an EPI sequence (right). Adapted from (32).

Using EPI, it is possible to image one slice in about 50-100 milliseconds, meaning that a whole head volume can be imaged in less than 10 seconds. The chief advantage of EPI is its rapid acquisition time. The short acquisition time reduces sensitivity to motion and enables time-resolved MR imaging. EPI sequences form the basis of functional MRI (fMRI).

However, due to the lengthy signal readout following a single RF excitation pulse, phase error will accumulate and cause geometric distortions. Geometric distortion is especially problematic in areas near air-tissue interfaces, where there are large magnetic field inhomogeneities (33).

4.1.7.1   Time-Averaging in Echo Planar Imaging

Owing to its short acquisition time, many EPI scans can be repeated within the time necessary to complete one single GRE scan. Multiple time repeats of EPI sequences can be averaged to increase SNR. Similarly, multiple susceptibility maps, each produced from a single EPI time point, could be averaged together to produce one susceptibility map with higher SNR.

4.1.8   Parallel Imaging

One strategy for reducing acquisition time is known as parallel imaging (PI). When PI is employed, the phase-encoding direction is undersampled by only reading a proportion of the phase encoding lines, thus acquiring a reduced amount of *k*-space data points. Aliasing may occur due to the undersampling. PI algorithms then reconstruct full FOV images from the limited *k*-space data by using information about the individual coil sensitivities of the RF coils (34).

Importantly for GRE imaging, when resolution is kept constant, PI results in faster image acquisition. Importantly for EPI, PI methods reduce the echo train length, which reduces distortions and susceptibility artifacts due to T_2* decay (35). PI methods have been shown to increase functional localization of brain structures due to decreased geometric distortions (36). One common PI method that is implemented on Siemens scanners is generalized autocalibrating partially parallel acquisitions (GRAPPA) (37).

4.1.9   2-D vs 3-D Imaging

2-D or 3-D imaging refers to the method of slice excitation in a sequence. In 2-D imaging, one thin slice is selectively excited, and the *k*-space matrix is filled for that slice before a new excitation frequency is selected and a new slice is excited. While the slice has a thickness typically on the order of 1 to 2 mm, and thus contains voxels instead of pixels, it is nevertheless referred to as a 2-D slice. In 2-D imaging, slice thickness is limited by SNR and scanner hardware-limited field gradient sizes.

3-D imaging can have non-selective or selective excitation. In non-selective excitation, there is no slice gradient and the entire volume is sensitive, whereas, in selective excitation, there is a slice gradient and a thick volume, or slab, is excited. Reconstructed slices within the 3-D slab are identified through partition encoding, isolated by their respective phase encoding gradient settings. Every RF excitation pulse excites the entire slab, but only a particular region's signal is recorded at any given time.

3-D imaging offers several advantages over 2-D imaging, including flexibility in slice thickness, better resolution in slice thickness direction, and shorter TEs. Higher resolution and shorter TEs lead to greater signal because of less T_2* dephasing, thus 3-D sequences generally have higher SNR. However, 3-D sequences suffer from longer acquisition times and increased susceptibility to motion artifacts (26).

4.1.10 Magnitude & Phase Images

MR signal is inherently complex, containing a magnitude and a phase component. This results from quadrature detection, where signal is detected in two orthogonal directions. The phase indicates the direction of the signal vector in quadrature detections. Traditionally, only the magnitude images were considered diagnostically useful. However, phase images can be useful

in showing contrast between tissues with varying magnetic susceptibilities via the effect that these have on the local static magnetic field. Several important MR methods, such as susceptibility weighted imaging (SWI) and QSM, rely on phase data. SWI uses phase data to increase contrast of magnitude images, especially between venous blood, iron deposits, and surrounding tissue (38). QSM uses exclusively phase data to reconstruct a map of local tissue susceptibilities (20).

In GRE images, phase images represent magnetization of the sample, which depends on local magnetic susceptibility.

Phase maps have become more useful as high field and ultra-high field scanners have become more prevalent, because magnetic susceptibility effects are proportional to field strength. Additionally, multi-channel receive coils aid in SNR of phase images, further increasing their viability as diagnostically useful images (39).

4.1.11 High field & Ultra-High Field Imaging

Field strength is a primary classifier of an MR scanner. High-field imaging refers to scanners with a static magnetic field strength of 3 Tesla or above, while ultra-high field imaging refers to a static magnetic field strength of 7 Tesla or above. Currently 1.5 T and 3 T scanners are most common for clinical purposes. There are currently about eighty 7 T scanners used for research around the world, and the first 7 T scanner was approved for clinical use in the United States and Europe in 2017 (40).

As seen in Equations 4.15 and 4.16, MR signal is proportional to static field strength B_0. Ultra-high field strength scanners will produce higher SNR images when all other parameters are kept the same. Increased SNR allows for higher resolution and contrast, especially between gray and white matter. T_2* contrast is improved at 7 T because slight differences in magnetic susceptibility cause faster phase development, and are thus more detectable (41).

Resolution at 7 T can reach roughly 0.5 mm isotropic, while 3 T scanners typically produce high quality images at most at 1.0 mm isotropic. Higher resolution allows for increased visualization of detailed brain anatomy, including cortical lesions, and may aid in diagnosing common neurological disorders (42).

Increased field strength also allows an image with fixed resolution to be acquired faster. Shorter acquisition time is beneficial to reduce motion artifacts, minimize patient discomfort, and improve economics of MR scanning.

4.2   Quantitative Susceptibility Mapping

QSM is a method to calculate the spatial distribution of local tissue magnetic susceptibility in MR images. Magnetic susceptibility is an intrinsic, material-specific measure of the extent to which a material becomes magnetized in an external magnetic field. QSM uses MRI phase data because the phase map reflects the local static magnetic field and can be used to calculate local magnetic susceptibility (20). Constructing a susceptibility map requires coil channel combination, phase unwrapping, brain masking, background field removal, and solving the ill-posed dipole field inverse problem (8).

QSM provides contrast between gray matter (GM), white matter (WM), myelin, and iron, as well as other bodies with varying susceptibility values. This enables many brain structures, including those in the brainstem, to be visualized with more clarity than is possible in T_1- and T_2*-weighted images (43).

While the previously established method SWI uses susceptibility to increase contrast, it does not provide quantitative measures of susceptibility. The key improvement of QSM in comparison to SWI is that it provides quantitative, isotropic measures of magnetic susceptibility (44).

However, the assumption that susceptibility sources does not hold for all tissue types in the brain. For example, the susceptibility of white matter tracts can be anisotropic according to the shape of myelin sheaths surrounding the tracts. Susceptibility Tensor Imaging (STI) is a method related to QSM that takes the anisotropic nature of susceptibility into account in order to map 3-D pathways and orientation of white matter tracts (45).

Other factors that affect the quality of QSM images include chemical shift effects from fat and patient-specific challenges, such as movement in the scanner, physiological motion, cranial blood flow, and blood oxygenation levels (46).

The QSM field does not yet have fully standardized protocols, making inter- and intra-subject reproducibility an issue, especially across pipeline strategies between imaging centers and scanning hardware (44). While QSM has not yet been standardized and validated to be adopted widely on clinical systems, the field is developed enough for physicians to consider including QSM in their routines by saving automatically magnitude as well as phase images from all gradient echo sequences in their protocols (47).

4.2.1 *Magnetic Susceptibility*

Magnetic susceptibility is a physical property of materials. It is the magnetization of a material in the presence of an applied magnetic field, defined as the scalar ratio of magnetization, *M*, to applied magnetic field intensity, *H*, according to[3]

$$\chi = \frac{\vec{M}}{\vec{H}} \tag{4.28}$$

where both *M* and *H* are measured in Amperes per meter, indicating that χ is dimensionless. For the purposes of MRI, susceptibility is often described in parts-per-million (ppm).

When a material's induced magnetization is in alignment with the external magnetic field, χ is positive and the material is known as paramagnetic. When a material's induced alignment is against the external magnetic field, χ is negative and the material is known as diamagnetic. Paramagnetic materials are drawn towards the magnetic field while diamagnetic materials are repelled away from the field. The material's own magnetic moment interacts with the external field, with paramagnetic materials increasing the concentration of magnetic field lines and diamagnetic materials reducing their concentration, as shown in Figure 8. Calcium, oxyhemoglobin, myelin, and water are common diamagnetic materials while iron, deoxyhemoglobin, and air are common paramagnetic materials. The largest susceptibility difference in MR imaging is that between biological tissue and air, while most of the useful contrast in QSM images comes from variation in myelin and iron content (48).

---

[3] Unless otherwise noted, all equations and theory until Section 4.2.7 are derived from Deistung et al. "Overview of quantitative susceptibility mapping."
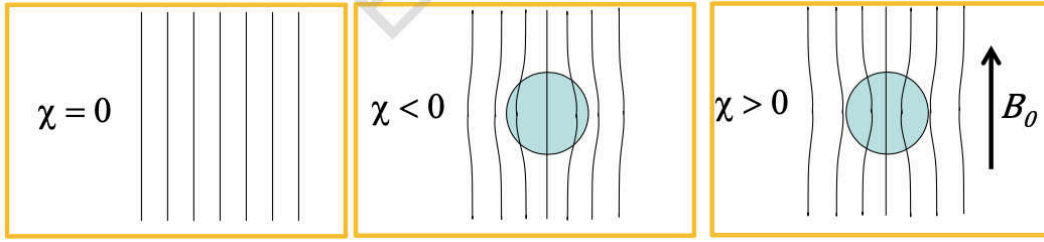
Figure 8: Classification of susceptibility. In the absence of susceptibility, a uniform magnetic field will have a uniform distribution of magnetic field lines (left). In the presence of a diamagnetic object, an opposing force is at work and the magnetic field lines separate (middle). In the presence of a paramagnetic object, an attracting force is at work and the magnetic field lines are drawn closer together (right). Adapted from (48).

Magnetic susceptibility is a bulk property, the mean of many molecules' responses to an external field. Most susceptibility contributions come from a material's electrons. In vivo, susceptibility can be both anisotropic and isotropic. Examples of biological tissues with anisotropic susceptibility include lipid bilayers, muscle fibers, and, most importantly for brain MRI, white matter fiber bundles.

Magnetic susceptibility at every point source in a volume induces field variation, $\Delta \vec{B}$, in the presence of an external magnetic field, due to the magnetization, $\vec{M}$, of the tissue. Field variation at each point $\vec{r}$ is defined by

$$\Delta \vec{B}(\vec{r}) = \frac{\mu_0}{4\pi} \iiint \nabla \times \left[\frac{\vec{M}(\vec{r'}) \times (\vec{r} - \vec{r'})}{\left| \vec{r} - \vec{r'} \right|^3} \right] d^3 r'. \qquad (4.29)$$

In cases when the main field is oriented only in the z-direction, the equation can be simplified to

$$\Delta \vec{B}_z(\vec{r}) = \mu_0 \int M_z(\vec{r'}) d_z(\vec{r} - \vec{r'}) d^3 r' \qquad (4.30)$$

where $d_z(\vec{r})$ is the point-dipole response of the magnetic field, defined by

$$d_z(\vec{r}) = \frac{1}{4\pi} \cdot \frac{3\cos^2\theta - 1}{|\vec{r}|^3} = FT^{-1}\left(\frac{1}{3} - \frac{k_z^2}{|\vec{k}|^2} \right). \qquad (4.31)$$

$D_z(\vec{r})$, above, is shown both in image space and k-space, where FT is the Fourier Transform and θ is the angle between $\vec{r}$ and $\vec{B}_z$. When magnetic susceptibility is sufficiently small, as is the case with biological tissue in the brain, the approximation

$$\mu_0 M_z(\vec{r}) \approx B_0 \chi(\vec{r}) \qquad (4.32)$$

holds true, leading to

$$\Delta \vec{B}_z(\vec{r}) = B_0 \int \chi(\vec{r'}) d_z(\vec{r} - \vec{r'}) d^3 r'. \qquad (4.33)$$

In k-space, field variation relates to magnetic susceptibility by

$$\Delta \vec{B}_z(\vec{k}) = B_0 \chi(\vec{k}) d_z(k) = B_0 \chi(\vec{k}) \left(\frac{1}{3} - \frac{k_z^2}{|\vec{k}|^2} \right). \qquad (4.34)$$

Solving the above relation for susceptibility is known in QSM as the inverse problem. It is ill-posed because the point-dipole response in Eq. 4.31 contains zeros for two conic surfaces at

the magic angle. The ill-posed nature of the inversion problem presents difficulties for calculating susceptibility maps, discussed further in Section 4.2.6.

Lastly, because the Larmor frequency of a given tissue is determined by the local magnetic field, measured frequency variation can be used to infer magnetization-induced magnetic field variations according to

$$\Delta f(\vec{r}) = \frac{\gamma}{2\pi} \Delta \vec{B}_z(\vec{r}). \tag{4.35}$$

Thus, phase development of an MR sequence relates proportionally to field variations and can be used to determine local susceptibility, according to

$$\varphi = \varphi_0 + 2\pi\gamma T_E \Delta B_z \tag{4.36}$$

where φ is the measured phase, φ_0 is the phase offset of the receiver coil, and T_E is the echo time. Therefore, susceptibility can be calculated based exclusively on the phase data of an MR image.

GRE sequences produce T_2*-weighted images, which have contrast resulting from local tissue inhomogeneities of magnetic susceptibility. While the contrast may arise from local field inhomogeneities, the T_2*-weighting itself is nonlocal. GRE images may include contrast in locations that do not contain susceptibility sources when they are neighboring regions with high susceptibility. T_2* contrast depends strongly on scan parameters and thus are qualitative instead of quantitative. It is also an anisotropic signal, varying according to the orientation of the sample volume. Susceptibility variation perpendicular to the static magnetic field appears stronger than susceptibility variation parallel to B_0.

QSM's key improvement over T_2*-weighted GRE images is the localization and quantization of susceptibility source distribution by inferring susceptibility from phase development (47).

4.2.2 Coil Combination

Modern MR radiofrequency receive coils are often made up of many small radiofrequency coils in a "phased-array" arrangement (39). The signals from the small coils are combined to produce a final composite image. Phased-array receive coils have the advantage of higher SNR than volume coils and enable parallel imaging acceleration. Each channel in the receive coil acquires the signal across the entire field of view (FOV) with different sensitivities based on its position relative to the sample. Combination of coil channels is an especially important precursor to QSM and is a non-trivial task for two reasons. First, each channel is subject to a unique, spatially varying (and generally unknown) phase offset (the phase at time zero) and second, phase data is only defined in a 2π range and thus experiences wraps in the image where phase development is outside the range $-\pi \rightarrow +\pi$. The phase offset value is made up of all time-independent components of phase signal, including the wavelength of the MR signal, the relative position of source and coil, eddy currents, and coil sensitivity (49).

Because QSM relies exclusively on phase information, accurate coil combination is a necessary first step of the process. In addition to proper phase matching between coils, no other phase variation may be present, as it would affect the calculated susceptibility values. One coil combination method applicable to multi-echo GRE sequences is ASPIRE. ASPIRE can combine coil channels without a volume reference coil or a reference scan and can be completed before phase unwrapping takes place (50). While ASPIRE requires multiple TEs and is thus incompatible with EPI sequences, the phase offsets calculated during the multi-echo GRE sequence can be used for accurate coil combination in EPI sequences as long as the matrix size, resolution, and position of the two sequences all remain identical.

4.2.3 Phase Unwrapping

While phase development follows Equation 4.36, acquisition of phase data on the scanner is restricted to a range of 0 to 2π, corresponding to

$$\varphi_w(r) = [\varphi_0 + 2\pi\gamma T_E \Delta B_z(r)] \, mod \, 2\pi \qquad (4.37)$$

where $\varphi_w(r)$ is the wrapped phase at a given voxel. The modulo operator in the above equation is the source of phase aliasing, or "wrapping," where any phase development in the image above 2π is wrapped to stay within the two-radian interval. An unwrapped phase image will have discontinuities in its phase development, as seen in Figure 9.
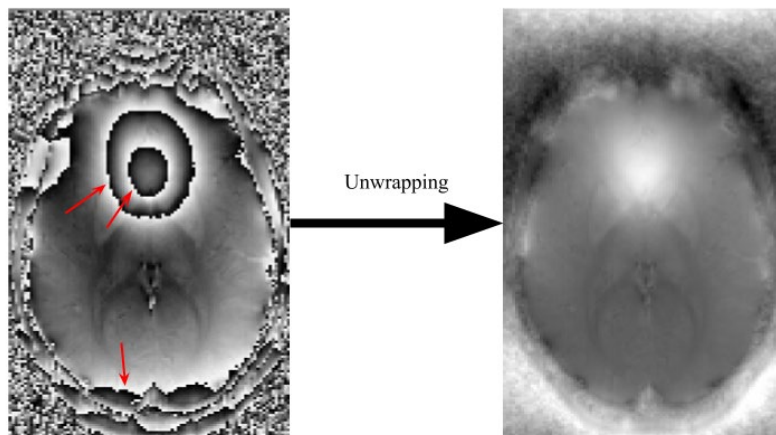

Figure 9: Example of phase unwrapping. The image on the left shows the raw phase output of the scanner, with several phase wraps evident (red arrows). The image on the right is the phase result after unwrapping. In this case, a Laplacian-based phase unwrapping method was used.

Sequences with longer TEs will have a higher number of phase wraps because there is more time for the phase to develop before signal acquisition. Sequences performed at higher field strengths will also have more phase wraps because phase develops faster under the influence of a stronger magnetic field.

The basic concept of phase unwrapping is to add *n* multiples of 2π to each voxel. However, the proper number of multiples for each voxel in the image must be determined in order to construct a map of the true phase.

Several strategies have been used to de-alias phase images. Temporal-based phase unwrapping techniques, such as temporal phase unwrapping (TPU) (51) and UMPIRE (52), determine wraps by analyzing the evolution of phase across two or more echo times. Spatial-based methods are image-based and analyze local phase behavior to identify large changes in phase value to identify wraps. They can be applied in two or three dimensions. Examples of spatial-based unwrapping methods include graph cut (53), 3-D best path (54), and region-growing (55,56) algorithms.

Temporal-based phase unwrapping techniques are more robust in the presence of many wraps and are less computationally expensive than spatial-based methods. However they come with the constraint of only working on multi-echo sequences (52).

A third option for phase unwrapping is a Laplacian-based method, which is path-independent and works for single echo data. Because of its robustness and relatively computational simplicity, Laplacian-based phase unwrapping is a popular method of phase unwrapping for QSM applications (57).

In Laplacian-based phase unwrapping, the true phase is represented as a function of the wrapped phase according to

$$\varphi(r) = \varphi_w(r) + 2\pi \cdot n(r) \tag{4.38}$$

where *n(r)* is

$$n(r) = \frac{1}{2\pi} \nabla_\perp^{-2} [\nabla_\perp^{-2} \varphi(r) - \nabla_\perp^2 \varphi_w(r)] \tag{4.39}$$

And $\nabla_\perp^2$ and $\nabla_\perp^{-2}$ are the forward and inverse two-dimensional Laplacian operators, the number of wraps *n(r)*, can be determined if the 2-D Laplacian of the unwrapped phase $\varphi(r)$ can be estimated. Note that $\varphi_w(r)$ is measured and does not need to be estimated. An estimate for the Laplacian of $\varphi(r)$ is

$$\nabla_\perp^2 \varphi(r) = \cos \varphi_w \, \nabla_\perp^2 (\sin \varphi_w) - \sin \varphi_w \, \nabla_\perp^2 (\cos \varphi_w) \tag{4.40}$$

This estimation of phase unwrapping is well-suited to phase maps in MRI and is resilient to noise in wrapped phase images (58).

4.2.4 Brain Masking

Before further processing can take place, a binary brain mask must be created to define the volume of interest (VOI) for background field removal and dipole inversion. The binary brain mask is a 3-D mask of the entire brain volume. Brain masks are generated from magnitude images, the only component of the QSM pipeline that relies on magnitude data. Brain masking is particularly important in QSM processing because unreliable voxels near air-tissue interfaces can have far-reaching affects inside the VOI, where imperfect brain masking leads to large, non-local variance in susceptibility maps (38) (59).

The Brain Extraction Tool (BET) (60) FMRIB Software Library (FSL) (61) is a robust segmentation method for isolating brain volumes from surrounding tissue. BET is fast, robust, and widely adopted.

Another option for brain masking is the segmentation tool in the SPM12 toolbox (62). Though slower and more computationally intensive that BET masking, SPM12 segmentation is more robust with EPI magnitude images than BET because it is optimized for fMRI pipelines. SPM12 segmentation separates inputs into 5 output images of WM, GM, cerebrospinal fluid (CSF), bone, and soft tissue.

4.2.5 Background Field Removal

MR phase images reflect the total magnetic field experienced by sample tissue in the VOI. Once the phase maps have been unwrapped, contributions to the magnetic field perturbation originating from outside the VOI, the background field contributions, must be removed. This is the chief goal of the background field removal step in the QSM pipeline.

Magnetic field perturbations propagate outwards from their sources and affect the magnetic field in the surrounding area. Therefore, while an MR image only acquires signal from within the chosen VOI, field perturbations due to structures outside of the VOI are superimposed on top of perturbations originating inside the VOI and appear in the MR image, as shown in

$$\Delta B_z(\vec{r}) = \Delta B_{local}(\vec{r}) + \Delta B_{bkgd}(\vec{r}). \tag{4.41}$$

Background field contributions are most often caused by the skull, paranasal sinuses, and torso, as well as by B_0 inhomogeneities and imperfect shimming values. Particularly, air-tissue

interfaces in the sinuses produce background field variation that extends deep into the brain (63). Once all background field contributions have been removed, the phase map is referred to as the local field map.

Early background field removal methods relied on the observation that background field variation has lower spatial frequency than local field and thus could be filtered out with a high pass filter (64,65). Drawbacks of those early techniques included the inability to filter out rapidly changing phase variations at air-tissue interfaces. An improvement utilized brain geometry to estimate and remove geometry-induced field changes caused by air-tissue interfaces before high pass filtering (59).

Three common approaches to background field removal in QSM are projection onto dipole fields (PDF), sophisticated harmonic artifact reduction for phase data (SHARP), and Laplacian boundary value method (LBV).

PDF utilizes the observation that a dipole source outside a given VOI induces a magnetic field that is roughly orthogonal to a magnetic field induced by a dipole inside the VOI (7). Thus the background field inside an VOI can be decomposed into a field made up of projections from dipole point sources originating outside the VOI (66).

SHARP recognizes that spatial distributions of magnetic field contributions in phase maps are harmonic functions that follow Laplace's equation. The mean value on a spherical surface is equal to the value at the center of the sphere. This assumption is used to improve the precision of background field removal (67). The size of the sphere, or kernel, can be varied to further improve SHARP, in a progress known as variable kernel SHARP or VSHARP (68).

Both PDF and VSHARP suffer from lower accuracy close to the boundary of the VOI. LBV assumes simple boundary conditions and removes the background field by means of solving the boundary value problems in Laplace's equations. This method preserves magnetic field data near the boundary (69).

In a different strategy, the integrated harmonic background phase removal using the Laplacian operator (iHARPERELLA) method combines phase unwrapping and background field removal into a single step and preserves tissue signal with excellent robustness (70).

One further challenge in background field removal strategies is the possibility of magnetic field perturbations affecting the magnetic field of neighboring tissues, such that one structure in the brain acts as a background field source to another structure in the brain. This would cause local field maps to contain spatially non-local information.

When background field contributions have been removed, the magnetic susceptibility can be expressed as

$$\Delta B_{local}(\vec{r}) = B_0 \cdot \int_{VOI} \chi(\vec{r'}) \cdot d_z(\vec{r} - \vec{r'}) d^3 r'. \qquad (4.42)$$

This local background field signal is a variation of Equation 4.33 that only includes local field contributions.

4.2.6 Dipole Inversion

As seen in Equation 4.42, the local magnetic field perturbation at a given point, $\Delta B_{local}(\vec{r})$, is a function of the bulk magnetic susceptibility, $\chi(\vec{r'})$, and the point-dipole response, $d_z(\vec{r})$. With this relation, the magnetic susceptibility distribution can be determined via a

deconvolution of $\Delta B_{local}(\vec{r})$ and $d_z(\vec{r})$. The deconvolution operator requires that the integral is evaluated over infinity, therefore $\tilde{\chi}(\vec{r})$ is chosen where

$$\tilde{\chi}(\vec{r}) = u(\vec{r}) \cdot \chi(\vec{r}) \tag{4.43}$$

and $u(\vec{r})$ is a function defined as

$$u(\vec{r}) = \begin{cases} 1 & within\ VOI \\ 0 & outside\ VOI \end{cases}. \tag{4.44}$$

The equation can be rewritten to solve for magnetic susceptibility as

$$\tilde{\chi}(\vec{r}) = (\Delta B_{local}(\vec{r}) \otimes^{-1} d_z(\vec{r})) \cdot B_0^{-1} \tag{4.45}$$

where $\otimes^{-1}$ is the deconvolution operator. Deconvolution can be carried out with the help of Fourier transforms, via

$$\tilde{\chi}(\vec{r}) = FT^{-1} \left\{ \frac{FT\{\Delta B_{local}(\vec{r})\}}{FT\{d_z(\vec{r})\}} \right\} \cdot B_0^{-1}. \tag{4.46}$$

This is the inverse problem for magnetic susceptibility, related to the inverse problem discussed in Section 4.2.1.

A key characteristic of Equation 4.46 prevents its evaluation for all values of $\vec{r}$. It is recalled that in Equation 4.31, that the point-dipole response of the field, $d_z(\vec{r})$, contains zeros on two conical surfaces, located at the so-called magic angle $\theta \approx 54.74°$. Because of these zeros, the inverse problem is ill-posed, meaning that it is underdefined and multiple solutions exists for one measurement.

Additionally, solutions to the inverse problem are especially sensitive to noise in regions near the conical surface, shown in Figure 10. Noise sensitivity often results in streaking artifacts that obscure small lesions and fine structure details.
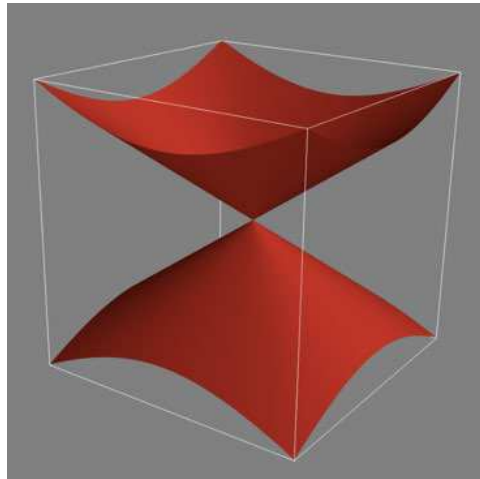
Figure 10: Visualization of two conical surfaces defined by the magic angle, $\theta \approx 54.74°$, the angle between B_0 and $\vec{r}$. On these conical surfaces, the inverse problem has no solution and thus the inverse problem is ill-posed. Adapted from (71).

One further difficulty arising from the inverse problem is that the k-space origin is undefined, and an unknown offset is applied to all values. This means that the susceptibility map lacks a true zero reference value and all susceptibility values must be referenced to a chosen region within the VOI. The reference region may be ventricular CSF or frontal WM, each of which has their own drawbacks and does not have uniform zero magnetic susceptibility (16,72).

Many methods have been developed to overcome this ill-posed susceptibility problem and fall into two main categories – repeated measurements at different orientations or regularization. Multiple measurements at different orientations is generally not feasible for *in vivo* MR imaging because of discomfort to patients (6,73). Regularization is a mathematical tool that selectively adds information in order to solve an ill-posed problem. Regularization is a trade-off between finding a better fit of the data and reducing the norm of the solution. Dipole inversion algorithms must balance streaking artifact suppression with smoothing of fine structure detail via the optimal level of regularization.

One of the first methods developed for dipole inversion is thresholded *k*-space division (TKD), which gained popularity for its relative simplicity. The dipole inversion equation is solved in *k*-space by inserting a constant value for a dipole kernel anywhere where the values are too small, below a certain threshold. TKD incorporates only general regularization and suffers from non-local artifacts arising from unreliable voxels (74).

One popular normalization-based method is morphology-enabled dipole inversion (MEDI). MEDI uses L1-norm minimalization as well prior information gained from the magnitude image. It takes voxels that are along edges in the susceptibility map but not along edges in the magnitude image and considers them sparse, before then completing L1 minimization. An improved MEDI with zero referencing using CSF is known as MEDI+0 (75).

A dipole inversion method that does not require prior information from the magnitude image is the iterative least-squares (iLSQR) approach. iLSQR creates an initial estimation of the magnetic susceptibility and the susceptibility boundaries, then uses an iterative approach to estimate and remove the susceptibility artifacts near the magic angle region. This method is effective at reducing streaking artifacts and allowing better visualization of fine structure detail (76).

A third dipole inversion strategy, named streaking artifact reduction in QSM (STAR-QSM), is a further improvement on streaking artifacts in iLSQR that is effective even for susceptibility maps with large dynamic ranges. STAR-QSM uses a two level regularization that independently solves for large and small susceptibility values based on a total variation optimization term (77).

Dipole inversion algorithms tend to be computationally intensive, which is a barrier to QSM becoming a clinical tool. QSM pipelines would need to be efficient and fast enough to run "online," i.e. on the scanner itself, and within a reasonable amount of time to be exported for the radiologist. One technique employing regularization, L(1)-regularized dipole inversion from the FANSI toolbox, was created to be fast enough to be implemented online (78).

The final resulting map of the dipole inversion step is the quantitative susceptibility map, where localized voxel-wise magnetic susceptibility values are depicted.

4.2.7 History and Development

While it began as a method for visualizing iron depositions without blooming artifacts that are inherent in SWI, QSM now enables highly localized quantitative measurements of susceptibility distributions. Pathologies for which QSM can be useful include neurodegenerative diseases, inflammation, hemorrhage, and irregularities in iron, calcium, and other metals (47). Developed in the mid-1990s, SWI was a precursor to QSM as it made use of phase image information for increasing contrast based on magnetic susceptibility. In 2001 first attempts were made to quantify susceptibility based on solving the inverse problem (79) but a significant breakthrough came in 2008 when Bayesian inference was used to account for

uncertainty in tissue structure and noisy data (7). In the past decade, the QSM field has greatly expanded, with numerous proposed solutions to background field removal and the inverse problem.

4.2.8   Current Applications

For all clinical applications of conventional GRE MRI, QSM can be used as well. Further, the method has potential applications beyond the capabilities of GRE and T_2* imaging. QSM can visualize micro-hemorrhaging in traumatic brain injury (TBI) (80), be used to detect lesions in MS (18), as well as evaluate changes in MS lesions over time, providing further insights into development of the disease (81). QSM has also been used for detection of calcifications (82).

Anatomical detail unavailable in conventional imaging contrasts are apparent in QSM, including cerebral substructures, deep gray matter structures, and brainstem nuclei (16,43). In fact, QSM presents promising opportunities for diagnosis of neurodegenerative diseases more generally. QSM has also been applied to studying iron concentrations in Alzheimer's Disease (83), Huntington's Disease (84), and Amyotrophic Lateral Sclerosis (ALS) (85).

Patients suffering from Parkinson's Disease may have increased iron concentrations in regions such as the subthalamic nucleus, which can be depicted better in QSM than in T_2*-weighted GRE images (86). Because small, iron-rich structures can be better visualized with QSM, the method may provide a critical improvement in neurosurgical planning and interventions such as deep brain surgeries (87).

4.2.9   Quantitative Susceptibility Mapping with Echo Planar Imaging

Though QSM has traditionally been carried out on GRE sequences, the relatively long acquisition time of GRE limits potential time-resolved susceptibility maps, presents time constraints in clinical settings, and is challenging for patients with neurodegenerative disorders such as PD or ALS. EPI sequences, with their acquisition time on the order of a few seconds, are good candidates for overcoming these challenges for QSM applications (88).   EPI sequences form the basis of a new application of QSM, functional QSM (fQSM) (89).

In comparisons between susceptibility maps derived from EPI and GRE datasets, EPI-QSM shows relatively more blurring due to lower spatial resolution and greater signal decay due to long readout time. As a consequence, microbleeds and calcifications may be difficult to see. However, EPI-QSM has been shown to provide clear contrast between iron-rich nuclei and surrounding tissue, proving its potential for imaging neurodegenerative disorders (88).

4.2.10 Super-resolution Quantitative Susceptibility Mapping

One promising future area of research is super-resolution reconstructed QSM. In 2-D EPI sequences, the slice thickness is often larger than the in-plane resolution. If a VOI is imaged multiple times with a slight spatial shift between acquisitions, the acquisitions can be combined to produce a reconstruction with much better through-plane resolution (90). As part of the FAST-STEM project at the High Field Imaging Center of the Medical University of Vienna, super-resolution QSM is being explored. Initial research has shown potential to improve localization of brainstem structures (91).

4.3   The Brainstem

The midbrain and two parts of the hindbrain, the pons and the medulla, make up the brainstem. The midbrain, pons, and medulla form, in descending order, an elongated structure extending from the cerebrum to the spinal cord. The pons serves as a connection between the brainstem and the cerebellum. It contains a thick mass of white matter that connects its posterior surface with the cerebellum. The medulla, like the pons, is coated in white matter. It is continuous with the white matter of the upper end of the spinal cord. Of most importance in this study, the midbrain contains several nerve bundles, known as nuclei, including the red nuclei and substantia nigra pars compacta. Superior to these brainstem nuclei lie deep subthalamic, iron-rich structures such as the globus pallidus, subthalamic nucleus, caudate nuclei, and putamen.

The general role of the brainstem is conveyance of nerve signals, with the area serving as a conduit for the major pathways between the brain and the spinal cord. It also hosts several cranial nerves and plays a regulatory role in some cardiovascular and respiratory functions (92).

4.3.1   Deep Brain Stimulation

Susceptibility maps are especially well-suited to visualize iron-rich structures and other deep brain regions such as GP, STN, and SNpc (16,86,93), which are common targets for DBS. DBS is a surgical intervention to reduce severe tremors, motor impairment, and gait difficulties in PD and other neurological disorders (94). High frequency stimulating electrodes are implanted in the STN, GP, or ventral intermediate thalamic nucleus. Though electrical stimulation of the brain has been performed for more than a century, the mechanism of DBS is not fully understood and is still being studied. Clinical effects of DBS are highly dependent on electrode placement, where tremors in certain regions of the body may be modulated based on stimulation of a particular brain nucleus (95). Current best practice is to use general atlas-based targeting (96). QSM may provide neurosurgeons with customized maps of DBS targets as part of their preoperative planning. Accuracy of electrode placement has been shown to be a strong indicator for DBS efficacy (97).

QSM of the midbrain in PD patients has already been studied (17,98,99), though all studies used phase data from 3-D GRE sequences for QSM.

Application of EPI-QSM as preoperative planning for DBS could result in reliable localization of target structures with increased patient comfort and shorter scan times.

4.3.2   Imaging Challenges

The brainstem nuclei, along with neighboring nuclei found in the subcortical region of the cerebrum, can be challenging to image. The brainstem is relatively small, making up less than 3% of total brain volume. The average diameter of an adult midbrain is about 18 mm, while brainstem nuclei are typically only a few millimeters wide. Because of its location deep inside the head, it can be difficult to simultaneously achieve high enough SNR and voxel resolution to obtain useful images.

The brainstem is also susceptible to a high level of physiological noise. The static magnetic field, B_o, will change due to chest motion, thus causing instability of MR images. Close proximity to arteries, CSF spaces, and parenchyma causes pulsatile artifacts.

GM and WM are less clearly separated in the brainstem than in the cerebrum and cerebellum. They are typically interwoven in complicated patterns of folds and layers smaller than the resolution of MR images, resulting in images showing the brainstem with falsely homogenous anatomy. (100)

4.3.3 Thesis Aims

Quantitative susceptibility mapping based on EPI sequences allows for rapid acquisition that is unattainable in conventional GRE-based QSM. An acquisition time is on the order of only a few seconds would lower scanning costs in a clinical setting; minimize discomfort to patients, especially those suffering from neurodegenerative disorders; and enable time-resolved susceptibility maps to be produced. Additionally, the short acquisition time reduces sensitivity to motion, a key factor in PD patients experiencing tremors.

However, EPI suffers from geometric distortions, especially near tissue-air interfaces where there are large magnetic field inhomogeneities. EPI has lower maximum resolution than similar GRE sequences, and produces images with lower SNR than GRE images of matching resolution.

The aim of this study was to develop a QSM pipeline suited specifically to 2-D EPI acquisitions at both high field and ultra-high field strength. Strategies were explored to overcome relatively lower SNR and geometric distortions inherent in EPI. Approaches were evaluated on their abilities to quantify local tissue susceptibility and localize subcortical brainstem nuclei, with the goal of yielding susceptibility maps of high enough quality to make rapid EPI-QSM imaging of brainstem nuclei feasible.

5 Methods

5.1 Data Acquisition

Measurements were carried out with one healthy volunteer at ultra-high field strength (7 T) and one healthy volunteer at high field strength (3 T). Measurements performed at 7 T were on a Siemens Magnetom scanner (Siemens Healthineers, Erlangen, Germany) with a 32-channel head coil (Nova Medical, Wilmington, MA, USA). Measurements at 3 T were on a Siemens Prisma Fit scanner (Siemens Healthineers, Erlangen, Germany) with a 64-channel head coil (Siemens Healthineers). All scans were of whole head volumes acquired with sagittal slices and monopolar readout, using a GRAPPA factor of 2 and partial Fourier of 6/8.

Field of view, matrix size, and slice thickness were kept identical for 2-D EPI sequences and 2-D GRE sequences at each field strength to enable direct comparison, while the 3-D GRE sequence was acquired at a higher resolution to serve as a gold standard. The scan parameters for each protocol is listed in Table 1 below.

Field Strength	Sequence	FOV (mm x mm)	Matrix Size	Slice Thickness (mm)	rBW (Hz/pixel)	TR (ms)	TE (ms)	No. of Echoes	FA	Scan Time (min:sec)	Partial Fourier	GRAPPA
3 T	2-D EPI	230x230	176x176	1.5	1095	8190	29	1	80	2:03 (12 repeats)	6/8	2
	2-D GRE	230x230	176x176	1.5	140	25	10, 20	2	87	3:09	6/8	2
	3-D GRE	230x230	224x224	1	240	25	10, 20	2	15	7:38	6/8	2
7 T	2-D EPI	220x220	192x192	1.5	1371	6400	25	1	90	0:38 (12 repeats)	6/8	2
	2-D GRE	220x220	192x192	1.5	170	25	10, 20	2	71	2:58	6/8	2
	3-D GRE	220x220	288x288	0.8	170	25	10, 20	2	10	9:33	7/8	2

Table 1: Scan parameter values for all protocols used in this study, where FOV is field of view, rBW is pixel-wise receiver bandwidth, TR is repetition time, TE is echo time, FA is flip angle, and GRAPPA is the acceleration/undersampling factor.

5.2 Online Reconstruction

The combination of phase images from the phased-array coils was performed online with the ASPIRE algorithm. The channel-dependent phase offsets were calculated with ASPIRE on the 2-D GRE acquisition and were saved for use in reconstruction of the EPI sequence with matching FOV, matrix size, and slice thickness.

The magnitude and coil-combined phase images were saved separately and exported from the scanner reconstructor for further offline processing.

5.3 Quantitative Susceptibility Mapping Pipeline

Exported magnitude and coil-combined phase images were used to test algorithms at each step in the QSM pipeline and develop an ideal complete pipeline. Susceptibility maps were calculated from resolution-matched 2-D EPI and 2-D GRE measurements, as well as from a 3-D GRE sequence, which was used as the gold standard for comparison.

Multiple algorithms were tested at each step in the QSM pipeline and the algorithm which yielded the highest quality result was selected from amongst them. The highest quality algorithms were those which yielded susceptibility maps with high SNR, low streaking artifacts, low smoothing artifacts, and accurate susceptibility values compared to the literature.

5.4   Brainstem Structure Localization

Susceptibility maps produced from the best possible QSM pipeline were evaluated in their ability to identify and localize six subcortical and brainstem structures, measured by their susceptibility values and their CNR compared to immediately surrounding tissue.

5.5   Further Experimentation

Protocols were devised to test scanning parameters according to the SNR of their resulting susceptibility maps and the CNR between key brainstem and subcortical structures and surrounding white matter.

5.5.1.1   Experiment 1: Time-averaging in Echo Planar Imaging

To test whether susceptibility maps of time-averaged EPI images have higher SNR than susceptibility maps of single time-point EPI images, multiple repeats of 2-D EPI sequences were scanned.

5.5.1.2   Experiment 2: Echo-averaging in multi-echo Gradient Echo Imaging

To test whether susceptibility maps of echo-averaged GRE images have higher SNR than susceptibility maps of single-echo GRE images, two-echo GRE sequences were used.

5.5.1.3   Experiment 3: High field vs Ultra-high Field Strength

To test which field strength, 3 T or 7 T, produced the best data for calculating susceptibility maps, nearly identical scanning parameters were used at both field strengths and the QSM results were compared.

5.5.1.4   Experiment 4: Super-resolution Quantitative Susceptibility Mapping

To test the feasibility of QSM on super-resolution reconstruction volumes, a super-resolution reconstruction of a human brainstem created by Ehrmann et al. (91) was analyzed.

6 Analysis

Data analysis in this project entailed applying, testing, and evaluating algorithms in each step in the QSM pipeline to transform coil-combined phase images at high field and ultra-high field into susceptibility maps. Further, susceptibility maps were evaluated in their ability to localize subcortical and brainstem nuclei by analyzing CNR and SNR under various conditions.

DICOM images reconstructed using the MRI image reconstructor were converted to 4-dimensional (x, y, z, time repeat; or x, y, z, echo) NIFTI file format using the MATLAB tool "DICOM Sort and Convert to NIFTI" (101). All image processing was performed in MATLAB R2017b (102) using in-house developed scripts and suites developed by other QSM research groups detailed in the following sections.

6.1 Quantitative Susceptibility Mapping Pipeline

The reconstructed images were processed according to the three main steps of the QSM pipeline: phase unwrapping, background field removal, and dipole inversion. In addition, a brain mask was created to define the local and background regions, which is used in the background field removal step. An overview of the full QSM pipeline is shown in Figure 11.

One initial step necessary for the QSM pipeline is coil channel combination of phase images in the phased-array coil used in this study. Because only one coil combination method, ASPIRE, was used, it is not included in this study's analysis.

Algorithms used in the QSM pipeline were sourced from the STI Suite (103), the MEDI Toolbox (104), and the FANSI Toolbox (78), and were implemented with the help of the SEPIA toolbox (105).

For each step of the QSM pipeline, intermediate results were analyzed qualitatively, while the final susceptibility maps were analyzed both qualitatively and quantitatively. Qualitatively, susceptibility maps were evaluated in their degree of smoothing, a result of excess regularization, and in their degree of streaking artifacts, a result of the underdetermined inverse problem. Quantitatively, susceptibility values for brainstem structures and gray matter were compared to reported values in the literature.
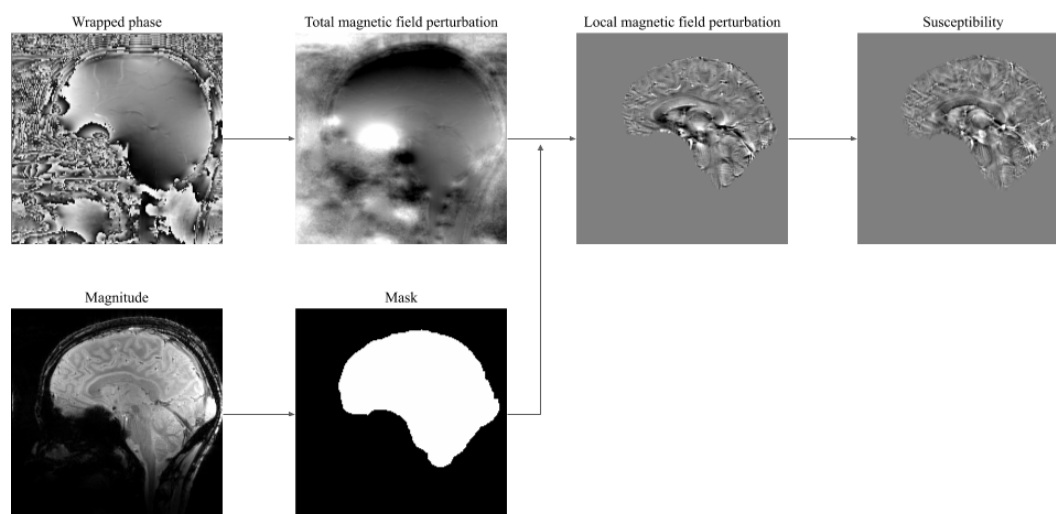

Figure 11: Step-by-step processes in the QSM pipeline. A brain mask is generated from the magnitude image. After coil combination of phase images (not shown), the combined phase image is unwrapped. The background field magnetic susceptibility contributions are then eliminated from the image, leaving the local field contributions as a local field map. The final step is the field-to-source dipole inversion that yields the susceptibility map.

6.1.1 Masking

Two binary brain masks were generated from the magnitude image. One was created using BET (fractional intensity threshold, f = 0.2; robust brain center estimation, R). The resulting BET mask was eroded using a 3-D kernel of size 5x5x5 voxels. Another binary mask was generated using the Segmentation Module from SPM12 (default inputs). Three segmented outputs—white matter, gray matter, and CSF—were pixel-wise added together and binarized. The binarized mask was dilated with a 3-D 5x5x5 voxel kernel and eroded with the same size kernel to fill small voxel holes inside the brain volume. The resulting binary brain mask was then eroded again using the 3-D 5x5x5 voxel kernel.

Both BET and SPM mask outputs were eroded with 3-D 5x5x5 kernels to eliminate voxels outside the brain from being included. A crucial consideration in the QSM pipeline is avoiding inclusion of background voxels because their susceptibilities will be propagated deep into the susceptibility maps as nonlocal contributions to the local field map.

Composite BET SPM masks were generated to take advantage of BET's accurate segmentation of brainstem and cerebellum from surrounding tissue and SPM's accurate segmentation of cerebral cortex from the surrounding subarachnoid space. A cutoff row was chosen as 10 mm above the base of the cerebrum. In the composite mask, all rows below the cutoff row were taken from the BET mask while all rows above the cutoff row were taken from the SPM mask.

All manipulations, unless otherwise noted, were carried out using FSLmaths, from the FSL package. An example of the BET and SPM masking pipelines can be seen in Figure 12.
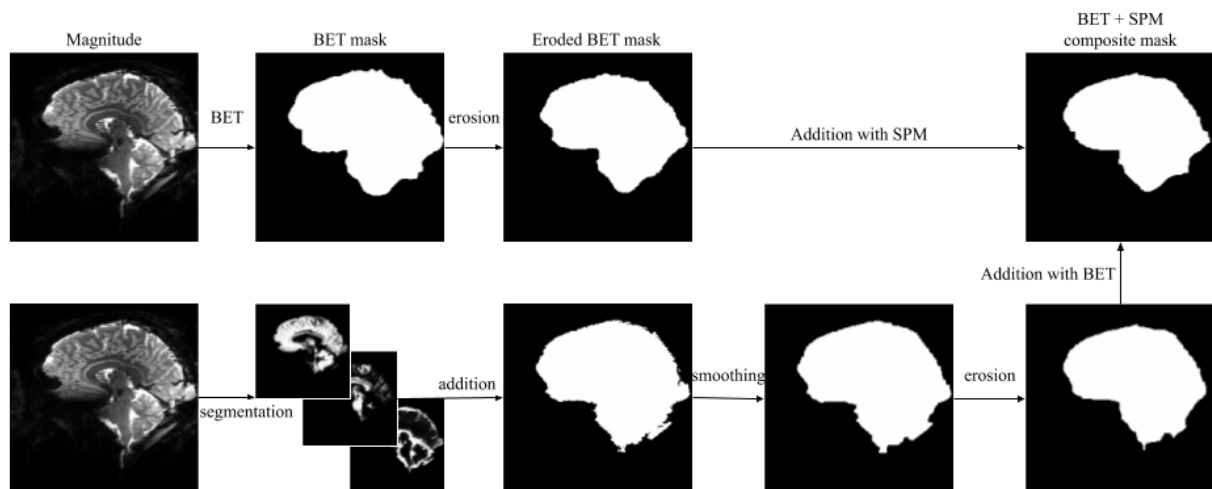

Figure 12: Step-by-step mask generation process. BET masking (top row) was a single automated step with the magnitude images as the input and the binarized mask as the output. This output was eroded to generate a mask less likely to contain background voxels. SPM masking (bottom row) required several steps. First, the magnitude image was segmented into five outputs of WM, GM, CSF, bone, and soft tissue. WM, GM, and CSF were combined and binarized. Small holes inside the brain volume were removed by a pair of dilations and erosions, and the product was then eroded to lower the likelihood of background voxels being included. Composite BET SPM masks were generated by choosing a cutoff row 1cm above the base of the cerebrum, then including the BET mask of all rows below the cutoff row and the SPM mask of all rows above the cutoff row.

The BET mask, eroded BET mask, SPM mask, eroded SPM mask, and composite BET SPM mask were tested to see which yielded best QSM results. Of particular importance to the masks was the exclusion of as many background voxels as possible while retaining important voxels near the brainstem.

The quality of masking was evaluated qualitatively based on visual inspection of the mask overlaid on the magnitude image. Masks that most closely matched the edge contour of the

brain in the magnitude image were of highest quality. Specifically, emphasis was put on the frontal border of the brainstem, region ventral to the subthalamic nuclei, and inferior border of the medulla. In EPI images, masks that accurately reflected geometric distortions, typically the frontal border of the front cortex and the frontal border of the medulla, were of highest quality.

Masks were also evaluated quantitatively by considering the accuracy of susceptibility values in their resulting QSM images.

Specifically, masks were rated according to how well they segmented brain tissue from surrounding tissue in the complex interface between brainstem and sinuses. Because many of the brainstem structures being analyzed in this study have complicated geometries located near the edge of the brain, precise masking was especially important to create useful susceptibility maps.

6.1.2 Phase Unwrapping

Phase unwrapping algorithms were used to remove phase aliasing, called wraps, from where the phase develops by more than 2π within the brain region, and to scale the result by the gyromagnetic ratio and TE. Phase unwrapping's output after scaling is a magnetic field perturbation map. The algorithms tested were a Laplacian-based phase unwrapping algorithm (68), ROMEO (106), SEGUE (56), Phi-UN region-growing (55), and graph-cut (53).

Resulting unwrapped phase images were qualitatively inspected for open-ended fringe lines and mismatched voxels. They were also inspected for contrast inside the brain region. SEGUE and Phi-UN phase unwrapping algorithms required a brain mask, while ROMEO, graph-cut, and Laplacian-based unwrapping did not.

6.1.3 Background Field Removal

Magnetic field perturbation maps underwent background field removal to eliminate contributions to the map that originated from outside the brain volume. In this step, the input, the magnetic field perturbation maps, is known as the total field map and the output, the perturbation map without background sources, is known as the local field map. Local magnetic field perturbation maps were calculated using iHARPERELLA, PDF, LBV, VSHARP, and a two-step variant of the VSHARP algorithm implemented in 2-D then 3-D.

The local field maps were visually inspected for behavior at the boundary of the volume of interest, especially in the border region near the brainstem, subcortical structures, and paranasal sinuses. Undesirable behavior included strong, diffuse signal that obstructed anatomical contrast within the brain.

Wei et al. (107), proposed a modified background field removal method, 2-D + 3-D VSHARP, specifically for 2-D EPI images at high field. This dual-step algorithm was tested on 2-D EPI images at both 3 T and 7 T. First, VSHARP was carried out on one slice at a time (2-D), then VSHARP was carried out on this intermediate local field map across multi-slice sections of the brain (3-D). The 3-D VSHARP removes through-plane harmonic components of the background field that are move evident in 2-D EPI acquisitions (107). This process was not applied to GRE images.

6.1.4 Dipole Inversion

The final step of the QSM pipeline, the field-to-source dipole inversion, converts the local magnetic field perturbation map into a magnetic susceptibility map. It was carried out with the following methods: STAR-QSM, iLSQR, MEDI+0, TKD, and L1-regularized dipole inversion from the FANSI toolbox.

Final susceptibility images were first evaluated qualitatively for streaking artifacts and how smooth the susceptibility maps were. Streaking artifacts result in incorrect susceptibility values propagated across the entire brain volume, typically rendering the entire brain volume unreliable. If a susceptibility map is too smooth, there may not be enough contrast to delineate small structures in the brain, which is especially important when analyzing brainstem nuclei.

The susceptibility images were then evaluated quantitatively comparing values to those in the literature. In a first run-through, susceptibility maps with regions of susceptibility higher than 0.20 ppm or lower than -0.20 ppm were considered incorrect. Susceptibility values in brainstem nuclei were then checked and compared to values given by Bilgic et al. (12).

6.1.5 Optimal Full Pipeline

After algorithms in each step of the QSM pipeline were evaluated and compared, an optimal QSM pipeline including phase unwrapping, masking, background field removal, and dipole inversion was found. The optimal full pipeline not only took into account the standalone quality of each pipeline step, but also the agreement of algorithms with each other through the entire pipeline to produce the highest quality final image.

6.2 Brainstem Structure Localization

Subcortical and brainstem structures were defined for use in calculating mean susceptibility values and contrast-to-noise ratios.

Bilateral regions of interest (ROIs) for the following brainstem and subcortical structures were drawn: caudate nuclei (CN), putamen (PU), globus pallidus (GP), internal capsule (IC), red nuclei (RN), and substantia nigra (SN). Each of the structures listed is paired in the brain, therefore each pair of structures was considered a single ROI. Each ROI was defined on a single slice, meaning that they were single-slice samples of the full structures. ROIs were drawn and analyzed using MRIcro (108).

In the 2-D GRE images, the ROIs were overlaid on three sets of echo-averaged susceptibility maps. In the 2-D EPI images, the ROIs were overlaid on three sets of time-averaged susceptibility maps. Because of distortion in the 2-D EPI images near several ROIs, ROIs were adjusted in both position and shape to better match the location of the structures in each measurement.

In the 3-D GRE images, to simulate three volumes, the ROIs were drawn across three slices within one volume of the echo-weighted susceptibility map.

An ROI was also drawn in cerebral white matter (CWM), to serve as the base for the noise measurement in CNR calculations.

The ROIs and their respective sizes in number of voxels are listed in Table 2. Note that ROIs were drawn separately for 3 T and 7 T datasets, as different healthy subjects, fields of view, and resolutions were used.

ROI	7 T			3 T		
	2-D EPI	2-D GRE	3-D GRE	2-D EPI	2-D GRE	3-D GRE
CN	62 voxels	61 voxels	171 voxels	53 voxels	53 voxels	189
PU	80	113	480	85	85	173
GP	105	161	583	96	96	154
IC	52	64	180	61	61	85
RN	25	28	98	32	24	45
SN	21	23	128	30	26	101

Table 2: List of subcortical and brainstem structures and their respective sizes, where CN is caudate nuclei, PU is putamen, GP is globus pallidus, IC is internal capsule, RN is red nuclei, and SN is substantia nigra. ROI sizes vary between 3 T and 7 T because different healthy subjects were measured.

In Figure 13, all subcortical and brainstem structures are shown for each sequence type at 7 T. In every image volume, IC, PU, CN, and GP were taken from one same slice, and SN and RN were taken from another slice. Note that geometric distortions in EPI images caused significant changes in ROI shapes relative to GRE images.
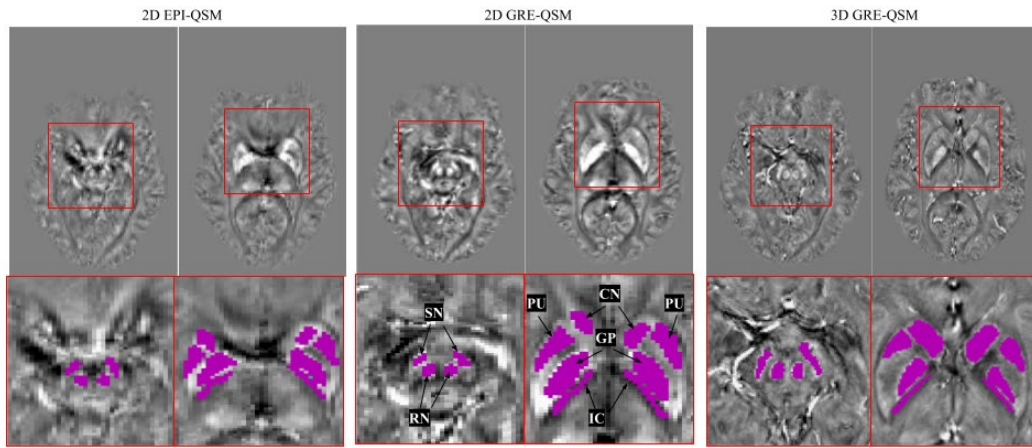

Figure 13: All ROIs used in susceptibility and CNR calculations for 2D EPI, 2D GRE, and 3D GRE susceptibility maps at 7 T. Labels indicate CN for caudate nuclei, PU for putamen, GP for globus pallidus, IC for internal capsule, RN for red nuclei, and SN for substantia nigra.

6.2.1 Magnetic Susceptibility

Mean magnetic susceptibility values and standard deviation values for all ROIs defined above were recorded. Susceptibilities were averaged between measurements for all 2-D EPI and 2-D GRE sequences, and between the three chosen slices within one measurement for 3-D GRE sequences.

6.2.2 Contrast-to-Noise Ratio

Mean susceptibility values from the ROIs as well as mean susceptibility values of tissue immediately surrounding each ROI were used to calculate contrast-to-noise ratios (CNRs) across the six brainstem structures defined above. For every ROI highlighted in Figure 13, a corresponding region of surrounding tissue was defined, and its average susceptibility measured. In Figure 14, the internal capsule ROI along with its surrounding tissue is shown as an example of the data collected for CNR calculations.
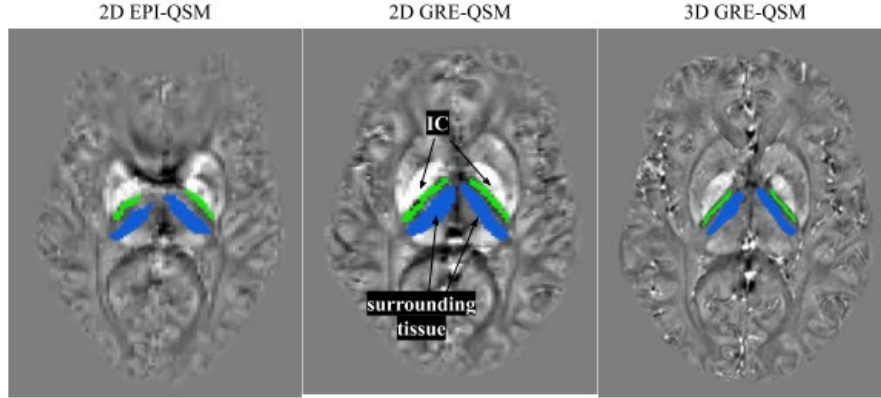
Figure 14: Example pair of the IC ROI (green) with region of surrounding tissue (blue), used to calculate CNR.

CNR was defined as:

$$CNR = \left| \frac{\mu(ROI) - \mu(Surr)}{\sigma(CWM)} \right| \qquad (6.1)$$

where $\mu(ROI)$ is the mean susceptibility value of the chosen ROI, $\mu(Surr)$ is the mean susceptibility of a similarly-sized ROI of directly neighboring tissue, and the noise, $\sigma(CWM)$, is the standard deviation of susceptibility values within an ROI drawn in a region of cerebral white matter.

6.3   Further Experimentation

6.3.1   Experiment 1: Time-averaging in Echo Planar Imaging

In 2-D EPI sequences, image volumes were split by time repeat into a set of 3-D volumes. At 3 T, twelve time repeats were acquired and at 7 T, three time repeats were acquired. The QSM pipeline was performed separately on each time repeat and the resulting QSM images were then averaged together, weighted by their respective magnitude images, according to

$$Time\ Average = \frac{\sum_{i=1}^{n} QSM_i \times Magnitude_i}{\sum_{i=1}^{n} Magnitude_i} \qquad (6.2)$$

where *n* is the total number of time points. The SNR of time-averaged QSM images was then compared to the SNR of single-time-point QSM images.

Improvement in SNR depending on n is proportional to $\sqrt{n}$. However, complications to this formula arise *in vivo* because of motion artifacts. The patient may move his head during or between measurements, which will cause blurring artifacts and reduce the clarity of signal when measurements are combined.

6.3.2   Experiment 2: Echo-averaging in multi-echo Gradient Echo Imaging

In the GRE sequences, the images volumes were split by echo number into a set of 3-D volumes. The multi-echo GRE sequences have two echoes each, at 10 ms and 20 ms. The QSM pipeline was performed separately on each echo and the resulting QSM images were averaged together, weighted by their respective magnitude images, according to

$$Echo\ Average = \frac{\sum_{i=1}^{n} QSM_i \times Magnitude_i}{\sum_{i=1}^{n} Magnitude_i} \qquad (6.3)$$

where n is the total number of echoes and i is the echo number. Echo averaged was weighted according to magnitude in order to prioritize regions in each echo where signal is highest. Signal is highest where the tissue's T_2* time is similar to the echo time.

The SNR of echo-averaged QSM images was then compared to SNRs of QSM images from individual echoes.

6.3.3   Experiment 3: High Field vs Ultra-high Field Strength

Susceptibility values and CNRs for ROIs were calculated for all three sequence types at both high field and ultra-high field strength. They were then compared according to field strength to determine which field strength is better at localizing subcortical and brainstem nuclei for each sequence type.

6.3.4   Experiment 4: Super-resolution Quantitative Susceptibility Mapping

Once an optimal QSM pipeline was found, it was applied to a super-resolution-reconstructed brainstem volume produced by Ehrmann et al. (91).

Ehrmann et al. acquired six pairs of 2-D GRE and 2-D EPI sagittally-oriented measurements of a partial brain volume that included the entirety of the brainstem, each offset 0.3 mm from each other in the through-plane direction. The scans had matching resolutions, with slice thicknesses of 1.5 mm. Through-plane super-resolution reconstruction was performed on the image sets by reconstructing a combined image set according to partial contributions from the slice-offset image volumes. The super-resolution images had an effective slice width of 0.25 mm.

The resulting susceptibility maps were not subject to an ROI analysis but were produced as a test case for potential future applications of this work.

7 Results

7.1 Quantitative Susceptibility Mapping Pipeline

Results for each step in the QSM pipeline are shown for one 2-D EPI measurement and one 2-D GRE measurement at ultra-high field.

7.1.1 Masking

Masking had a marked influence on the QSM results. Conservative masks, i.e. masks including some voxels outside of the brain volume, resulted in poor QSM images. Due to the harmonic nature of the background field removal algorithm, signal contained in the non-brain voxels that were not masked out affected the susceptibility values in regions far away from the edges of the brain. Masks that eliminated as many background voxels as possible while preserving the brainstem structures along the complex border between the brainstem and sinuses were most suitable.

SPM masking was more time intensive, as each volume took about 10 times longer to be segmented than for the BET process, about 3 minutes compared to about 15 seconds. SPM segmentation is implemented in MATLAB whereas BET is compiled C code. When the combination of SPM outputs is taken into account, masking with SPM involves many more steps than BET masking.

The BET-generated brain mask performed better than the SPM-generated brain mask around the brainstem, cerebellum, and neck region, especially in scans performed at 7 T, where there was some signal dropout in 2-D EPI images around the brainstem. The SPM mask tended to exclude regions near the dorsal end of the cerebellum and medulla. The SPM-generated mask performed better than the BET-generated mask around the cerebrum, especially in masking out cerebrospinal fluid signal in the subarachnoid space and central sulcus.

Because the BET mask was more effective at delineating the brain around the brainstem and cerebellum, and the SPM mask was more effective at delineating the brain around the cerebrum, the BET SPM composite mask proved to be most effective. The optimal cutoff plane between the two masks was defined as the row 10 mm above the inferior edge of the cerebrum.

The BET mask, SPM mask, and composite BET SPM mask, and their effects on local field maps and susceptibility maps can be seen in for a GRE image in Figure 15 and an EPI image in Figure 16.
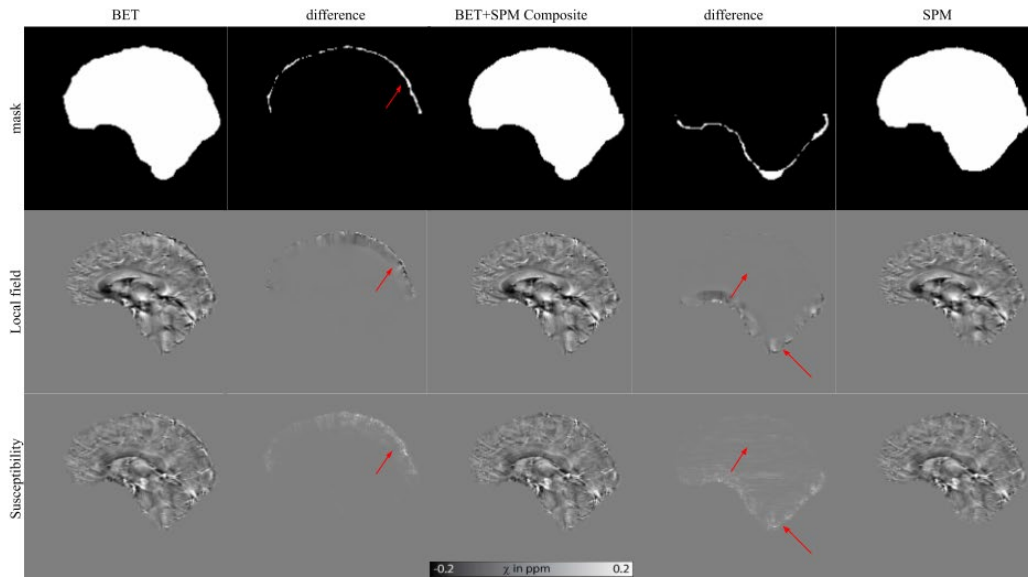
Figure 15: BET mask, SPM mask, and BET SPM composite masks and their effects on local field and susceptibility maps in GRE scans. In each of the difference masks, the white voxels indicated areas within the BET (or SPM) mask that were not included in the combined mask. In the difference images between BET and BET+SPM composite, the 2 extra voxels in the BET mask at the cerebral cortex results in changes to the local field map and susceptibility map across up to 15 voxels. Similar results are seen in the difference images between SPM and BET+SPM composite, where changes in the susceptibility map are seen across the entire brain volume, up to 50 voxels away from the masking differences.

Inclusion of background voxels in masks affects voxels far away from those near the border of the brain region. In susceptibility maps from GRE acquisitions, the majority of the differences were contained within a 10-voxel range from the mask border.

However, susceptibility maps were much more sensitive to masking effects for EPI images than for GRE images. The EPI images suffered from distortion both at high field and ultra-high field. The distortion was mainly located anterior to the pons and near the inferior portion of the anterior cortex. Geometric distortion introduced challenges to accurate brain masking.

The inclusion of background voxels propagated throughout the entire susceptibility map, as seen in Figure 16. Highly paramagnetic regions in the combined-mask QSM image (about 0.10 ppm) were approximately twice as paramagnetic in both the SPM-only and BET-only QSM images. A similar relationship held for diamagnetic regions, indicating that imperfect masking introduced incorrect scaling across the entire VOI, which was exacerbated by the dual-step 2-D and 3-D VSHARP background field removal method.

Though susceptibility maps from BET-only and SPM-only masks contained enough contrast around brainstem structures to delineate them, their susceptibility values were not reliable.
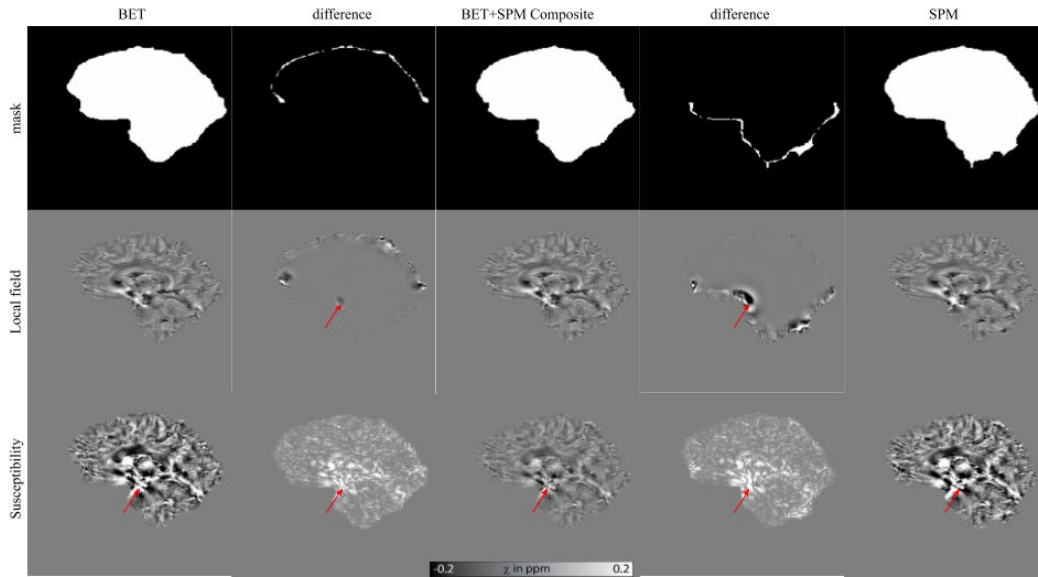
Figure 16: BET mask, SPM mask, and BET SPM composite masks and their effects on local field and susceptibility maps in EPI scans. In each of the difference masks, the white voxels indicated areas within the BET (or SPM) mask that were not included in the combined mask. The difference in local field maps indicate how inclusion of background voxels affects the local field map across nearly the entire volume. Susceptibility values in the SPM-only and BET-only masked QSM images were approximately double the susceptibility maps from the combined mask image across their entire volumes. Red arrows in each susceptibility map indicate the red nuclei, where the roughly doubled susceptibility values are seen. Red arrows in the two difference images of local field maps show where the wide variation in susceptibilities originates.

7.1.2 Phase Unwrapping

Outputs of Phi-UN region growing, SEGUE, ROMEO, graph-cut, Laplacian-based phase unwrapping are shown in Figure 17.

In EPI images, variation existed between outputs for each algorithm, most clearly illustrated in the way regions near the edge of the brain volume were handled. Unwrapped phase maps from SEGUE and Phi-UN algorithms did not include all voxels within the brain volume that were included in the brain mask. This exclusion of voxels prevents the next step of the QSM pipeline, background field removal, from reliably removing background field sources from SEGUE and Phi-UN unwrapped phase maps.

Contrast in regions near the brainstem is larger in Laplacian-based unwrapped phase maps than in ROMEO or graph-cut unwrapped phase maps. Higher contrast within the brain volume in combination with good agreement with the brain mask made the Laplacian-based algorithm the best choice for phase unwrapping EPI images in the QSM pipeline.

For GRE images, region-growing phase unwrapping algorithms, SEGUE and Phi-UN, accurately unwrapped the brain volume in border regions. ROMEO failed to accurately unwrap all voxels in the region with the highest number of wraps, near the brainstem. Quality of magnetic field perturbation maps based on all four other algorithms was comparable, as defined by agreement with mask-defined brain border and contrast within the brain region.
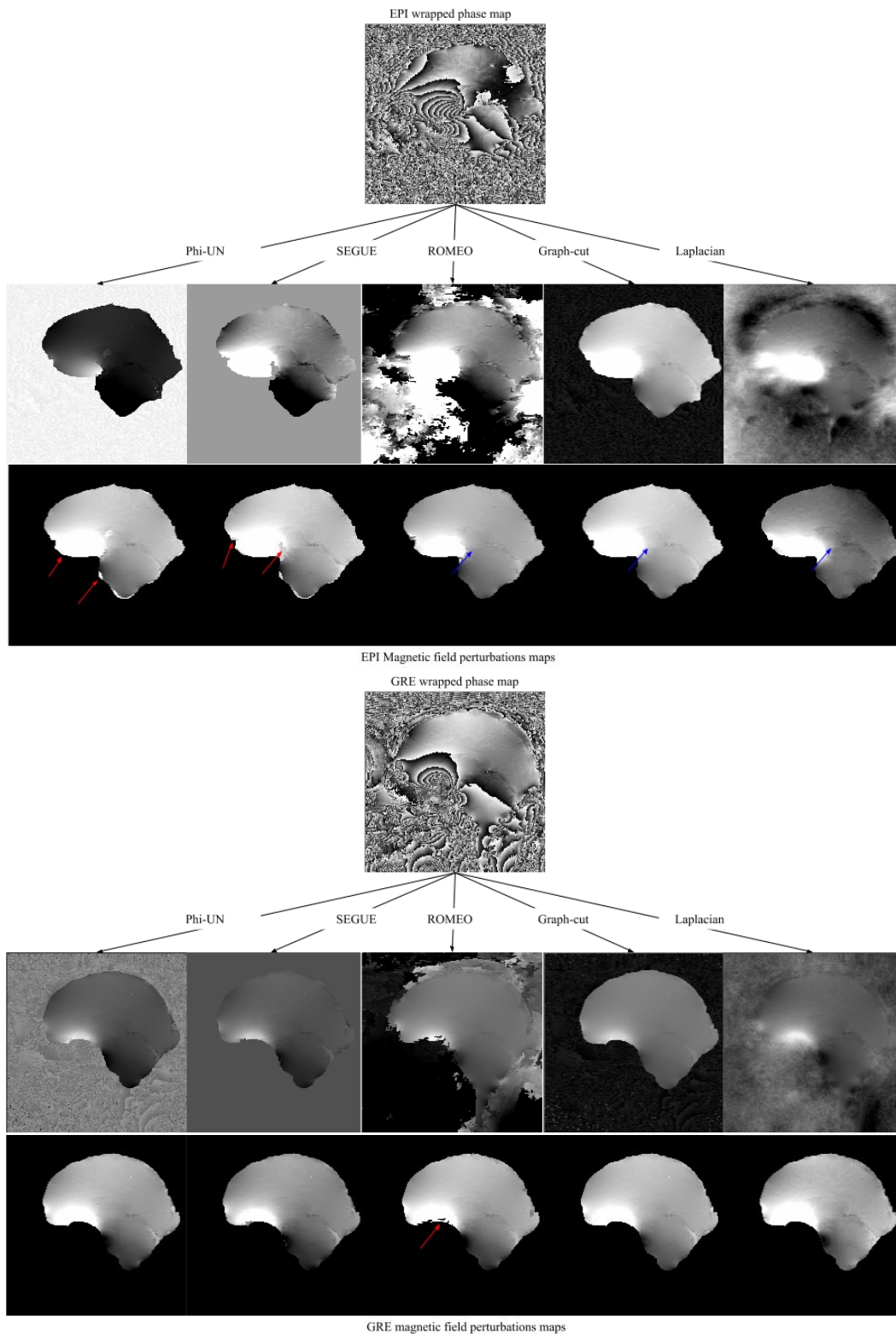
47

Figure 17: Magnetic field perturbation maps are calculated from raw phase data with phase unwrapping algorithms: Phi-UN, SEGUE, graph-cut, ROMEO, and Laplacian-based (EPI in upper-half, GRE in lower-half). For EPI, inconsistencies in unwrapped phase maps for the two algorithms that rely on brain tissue masks, Phi-UN and SEGUE, highlighted by the red arrows, show that not all voxels in the brain volume were included in the unwrapped images. Contrast in regions near brainstem structures is highlighted by blue arrows for graph-cut, ROMEO, and Laplacian-based unwrapped phase maps. Laplacian-based phase unwrapping preserved the most contrast within the brain volume. For GRE, ROMEO failed to properly unwrap several voxels at the brain-tissue interface near the brainstem, highlighted by the red arrow. Quality for all four other algorithms were similar.

7.1.3 Background Field Removal

A Laplacian-unwrapped total field perturbation map was used to test iHARPERELLA, PDF, LBV, VSHARP, and 2-D + 3-D VSHARP background field removal algorithms, with results shown in Figure 18. Images are arranged from left to right in order of increasing quality of EPI background field removal.

For EPI images, three of the five algorithms, iHARPERELLA, PDF, and LBV show clear blooming artifacts near the brainstem, indicating continued presence of background field signal. VSHARP and 2-D + 3-D VSHARP performed better at eliminating background signal, as local sources of high susceptibility are visually discernable in the local field maps.

Though blooming artifacts were lower for all algorithms in GRE images, VSHARP exhibited the least. Therefore, VSHARP produced the best background field removal for GRE sequences and 2-D + 3-D VSHARP for EPI sequences.
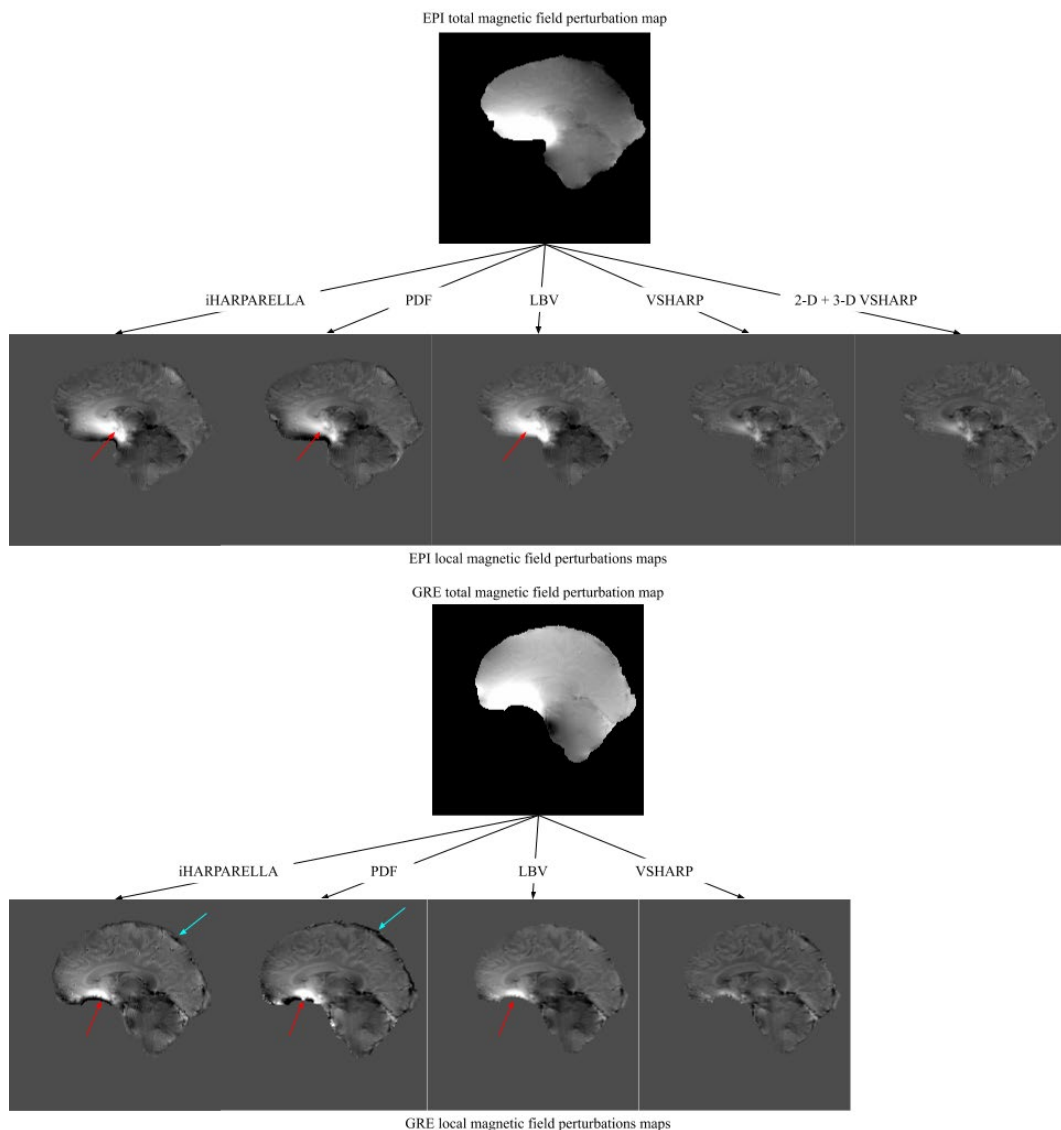

Figure 18: Local magnetic field perturbation maps are calculated from total magnetic field perturbation maps by separating the background field perturbation contributions from the contributions originating inside the brain volume, using iHARPERELLA PDF, LBV, VSHARP, and 2-D + 3-D VSHARP (EPI in upper-half, GRE in lower-half). Large, white blooming artifacts in iHARPERELLA, PDF, and LBV indicate incomplete removal of background signal (red arrows). For GRE images, artifacts are evident in the posterior cerebral cortex (blue arrows) for iHARPERELLA and PDF.

7.1.4 Dipole Inversion

Final susceptibility maps produced by solving the ill-posed dipole problem with MEDI+0, FANSI, TKD, iLSQR, and STAR-QSM are shown in Figure 19.

Two QSM algorithms were clearly inferior based on qualitative analysis. MEDI+0 produced a susceptibility map with extreme streaking artifacts, even when several regularization parameters were tested to find an optimal result. Inappropriate normalization within the FANSI dipole inversion produced a susceptibility map with significant smoothing artifacts. TKD, iLSQR, and STAR-QSM all produced susceptibility maps that were qualitatively acceptable. However, TKD suffered from poor contrast in the brainstem region, resulting in low contrast between brainstem structures and surrounding tissue. iLSQR and STAR-QSM produced the most accurate susceptibility maps. STAR-QSM yield susceptibility maps closer to literature values, while iLSQR tended to overestimate susceptibilities in both directions, i.e. paramagnetic regions were too paramagnetic and diamagnetic regions were too diamagnetic.
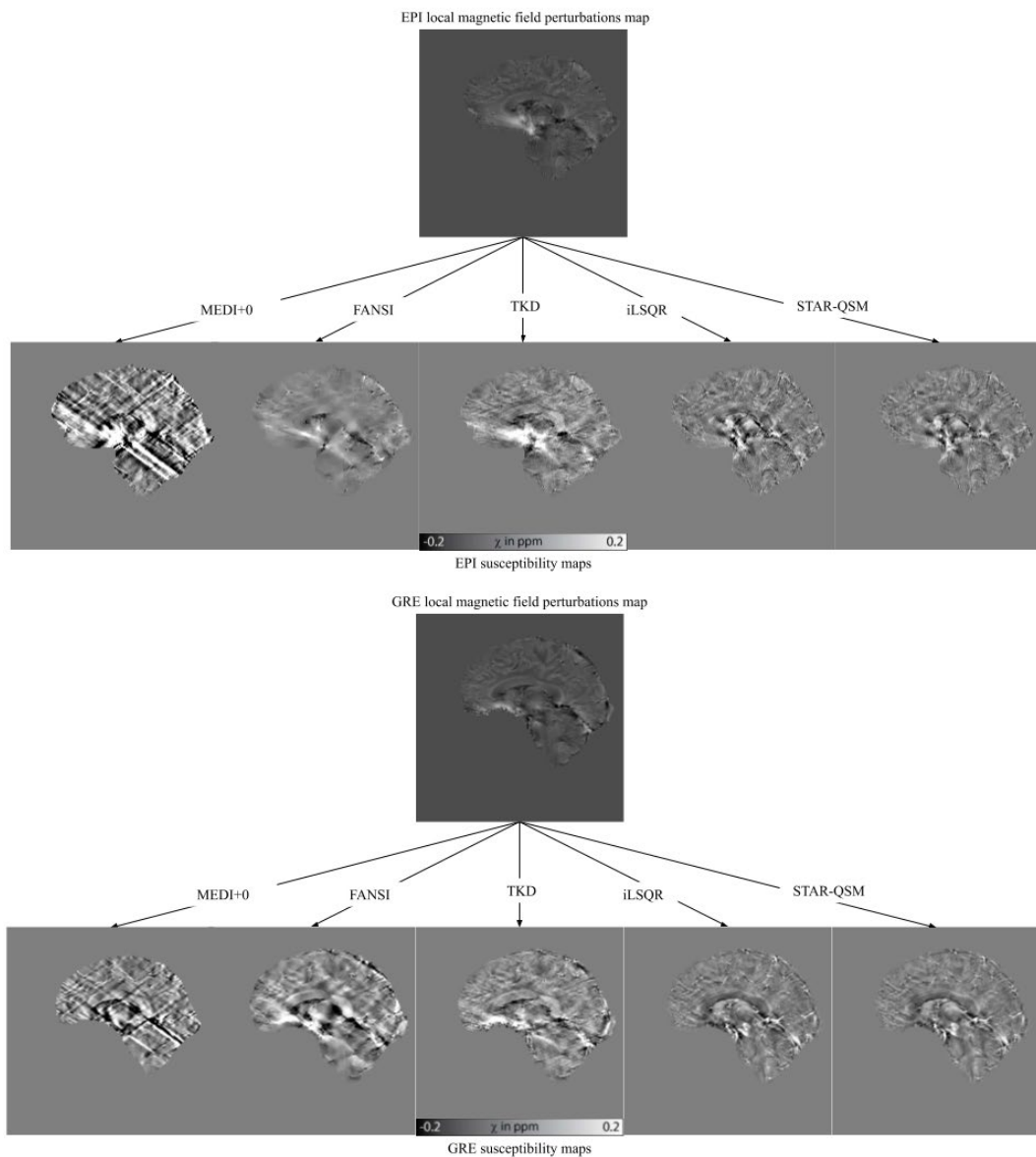

Figure 19: Final susceptibility maps produced by dipole inversion algorithms MEDI+0, FANSI, TKD, iLSQR, and STAR-QSM (EPI in upper-half, GRE in lower-half). Quality of susceptibility maps increases from left to right. MEDI+0 caused extreme streaking artifacts while FANSI caused excessive smoothing. STAR-QSM yielded susceptibility values closest to those in the literature.

7.1.5 *Optimal Full Pipeline*

The QSM pipeline that produced optimal results was Laplacian-based phase unwrapping, VSHARP background field removal, and STAR-QSM dipole inversion. All three steps of the QSM pipeline were implemented with the STI Suite. The optimal brain mask was a combination of a BET mask and an SPM mask. A susceptibility map for each sequence type at both field strengths generated with the optimal pipeline is shown in Figure 20.
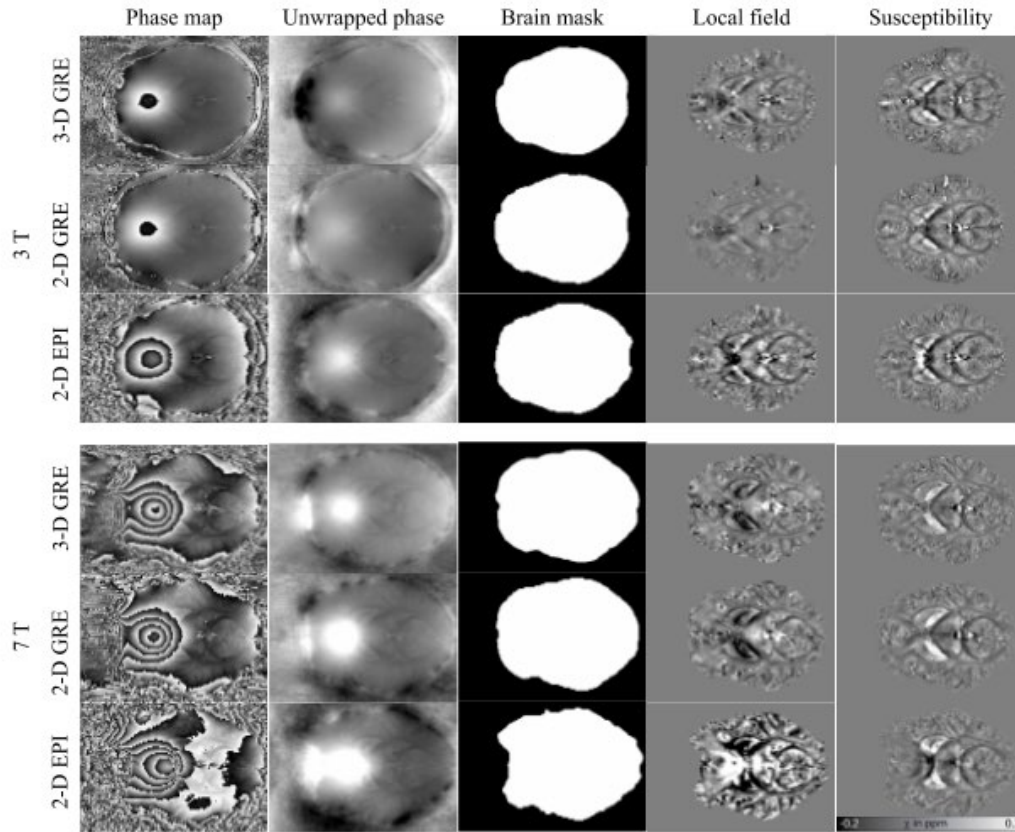

Figure 20: Optimal QSM pipeline and susceptibility map generated for each sequence type at high field and ultra-high field. Laplacian-based phase unwrapping, BET+SPM brain masking, VSHARP background field removal, and STAR-QSM dipole inversion were used. Geometric distortions in the EPI images caused irregular masks relative to their 2-D GRE and 3-D GRE counterparts at both field strengths.

7.2 Brainstem Structure Localization

7.2.1 *Magnetic Susceptibility*

Magnetic susceptibilities in ROIs of subcortical and brainstem structures are shown in Figure 21 and Table 3. Susceptibilities were in general agreement for every ROI across sequences, but significant variation remained. Error bars in Figure 21: S indicate error between multiple measurements of a single patient in a single scanning session.

No clear trend emerged of susceptibility values being consistently over- or underestimated in EPI-QSM images versus 3-D GRE-QSM images. Differences in susceptibility values were larger between 2-D EPI and the gold standard 3-D GRE then between 2-D GRE and the gold standard. Values only correlate strongly enough to indicate a general pattern of para- or diamagnetism in ROIs.

	7 T			3 T		
ROI	2-D EPI	2-D GRE	3-D GRE	2-D EPI	2-D GRE	3-D GRE
CN	0.072 ± 0.004	0.036 ± 0.001	0.019 ± 0.005	0.018 ± 0.003	0.028 ± 0.001	0.059 ± 0.004
PU	0.025 ± 0.001	0.023 ± 0.001	0.016 ± 0.004	0.036 ± 0.001	0.026 ± 0.001	0.031 ± 0.005
GP	0.082 ± 0.004	0.085 ± 0.002	0.061 ± 0.006	0.074 ± 0.001	0.085 ± 0.003	0.07 ± 0.016
IC	-0.027 ± 0.001	-0.043 ± 0.001	-0.046 ± 0.002	-0.066 ± 0.002	-0.055 ± 0.002	-0.065 ± 0.002
RN	0.043 ± 0.002	0.063 ± 0.002	0.053 ± 0.005	0.090 ± 0.001	0.074 ± 0.004	0.064 ± 0.002
SN	0.046 ± 0.002	0.066 ± 0.003	0.075 ± 0.016	0.103 ± 0.006	0.074 ± 0.001	0.101 ± 0.013

Table 3: Susceptibility values of subcortical and brainstem structures, averaged across three repeats. Susceptibility is in units of ppm. Standard deviation is of three measurement repeats conducted on a single healthy subject in a single session.
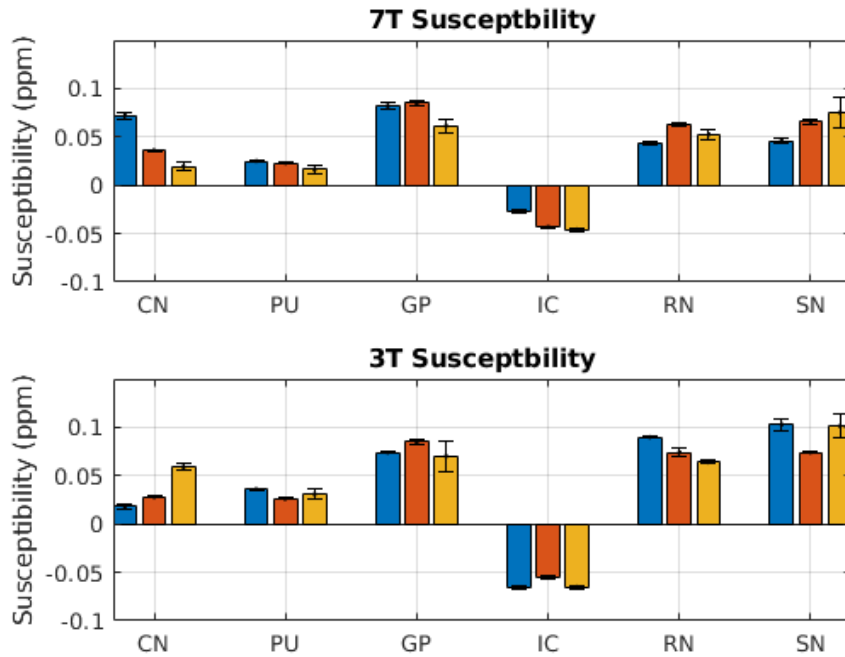

Figure 21: Susceptibility values for all ROIs from EPI-QSM (blue), 2-D GRE-QSM (orange), and 3-D GRE-QSM (yellow).

Differences from gold standard susceptibilities are shown in Table 4. Susceptibilities varied most widely at both field strengths for the caudate nuclei, where it was 4 times higher in EPI-QSM than in 3-D GRE-QSM at 7 T and nearly was 4 times lower in EPI-QSM than in 3-D GRE-QSM at 3 T. Susceptibilities matched the gold standard best at both field strengths of EPI-QSM for the putamen. EPI-QSM was generally closer to the gold standard at 3 T than at 7 T field strength.

	Difference in Susceptibility from 3-D GRE Gold Standard (ppm)			
	7 T		3 T	
ROI	2-D EPI	2-D GRE	2-D EPI	2-D GRE
CN	0.053	0.017	-0.010	-0.031
PU	0.009	0.007	0.010	-0.005
GP	0.021	0.024	-0.011	0.015
IC	0.019	0.003	-0.011	0.010
RN	-0.010	0.010	0.016	0.010
SN	-0.029	-0.009	0.029	-0.027
Average over all ROIs	**0.024**	**0.012**	**0.015**	**0.016**

Table 4: Differences in susceptibility values from the 3-D GRE gold standard for both EPI and 2-D GRE QSM images.

Susceptibility values for ROIs from EPI scans at 3 T were compared to literature values from Wei et al. (2017) and shown in Table 5 below. The values agreed most closely for the putamen, while the rest of the ROIs varied by approximately 0.02 ppm.

ROI	2-D EPI-QSM Susceptibility (ppm)		Difference (ppm)	Difference (%)
	This study	*Wei et al. (2017)*		
CN	0.018 ± 0.003	0.031 ± 0.006	-0.013	-53.1%
PU	0.036 ± 0.001	0.038 ± 0.005	-0.002	-5.4%
GP	0.074 ± 0.001	0.095 ± 0.008	-0.021	-24.9%
IC	-0.066 ± 0.002	−0.044 ± 0.005	-0.022	40.0%
RN	0.090 ± 0.001	0.075 ± 0.006	0.015	18.2%
SN	0.103 ± 0.006	0.076 ± 0.012	0.027	30.2%

Table 5: Susceptibility values for ROIs in this study compared to data from Wei et al. (2017). Both studies used the same phase unwrapping, background field removal, and field-to-source inversion. Susceptibility values are shown for EPI acquisitions at 3 T.

7.2.2 Contrast-to-Noise Ratio

All ROIs were qualitatively detectable from surrounding tissue, demonstrated by the CNR values shown in Figure 22 and listed in Table 6.

At ultra-high field strength, anatomical structures had generally lower contrast from their surroundings in EPI scans compared to 2-D GRE and 3-D GRE scans, except for the caudate nuclei. CNR in EPI-QSM was especially poor for the substantia nigra and red nuclei, owing to partial signal dropout and imperfect masking at 7 T. 2-D GRE outperformed EPI in CNR for every ROI except for the caudate nuclei.

At high field strength, CNR for EPI-QSM more closely matched the gold standard, and even provided better contrast than the gold standard for the red nuclei and substantia nigra. In absolute terms, CNR in EPI-QSM was higher at 3 T for five out of six ROIs and the average CNR across all ROIs was higher in EPI-QSM at 3 T.

2-D GRE-QSM had slightly higher average CNR across all ROIs at 7 T than at 3 T. At both field strengths, 2-D GRE-QSM CNR was higher than EPI-QSM SNR. The gold standard 3-D GRE-QSM suffered from low CNR at 3 T, even lower than EPI-QSM and 2-D GRE-QSM.

At both field strengths, the putamen exhibited the lowest CNR.

ROI	7 T			3 T			Average over sequences
	2-D EPI	*2-D GRE*	*3-D GRE*	*2-D EPI*	*2-D GRE*	*3-D GRE*	
CN	7.75 ± 0.85	4.38 ± 0.25	3.36 ± 0.83	3.00 ± 0.18	3.25 ± 0.13	3.86 ± 0.29	4.27
PU	2.69 ± 0.26	2.83 ± 0.07	3.00 ± 1.50	2.65 ± 0.13	1.21 ± 0.14	2.16 ± 0.34	2.42
GP	8.90 ± 0.10	10.75 ± 0.33	8.92 ± 1.37	6.07 ± 0.22	8.63 ± 0.33	5.00 ± 2.34	8.05
IC	2.87 ± 0.33	5.25 ± 0.13	7.02 ± 3.11	4.94 ± 0.13	5.79 ± 0.40	5.71 ± 0.89	5.26
RN	4.12 ± 0.38	8.79 ± 0.40	9.97 ± 4.13	7.98 ± 0.36	9.42 ± 1.05	4.06 ± 0.28	7.39
SN	4.36 ± 0.26	9.17 ± 0.14	11.50 ± 2.10	9.17 ± 0.08	9.33 ± 0.47	7.98 ± 0.68	8.59
Average over ROIs	5.12	6.86	7.30	5.64	6.27	4.80	6.00

Table 6: CNR values of subcortical and brainstem structures, averaged across three repeats, at both high and ultra-high field. Green color indicates that the CNR was significantly higher for that ROI at that field strength, Red color indicates inferior CNR, and gray color indicates similar CNR between field strengths. Out of all the measurements, average CNR across all brainstem structures was highest for 3-D GRE-QSM at 3 T and lowest for 3-D GRE-QSM at 7 T. Average CNR across all brainstem structures was higher at high field than ultra-high field for 2-D EPI. The red nuclei and substantia nigra were the most distinguishable from their surroundings across all measurement types, while the putamen was the least distinguishable.
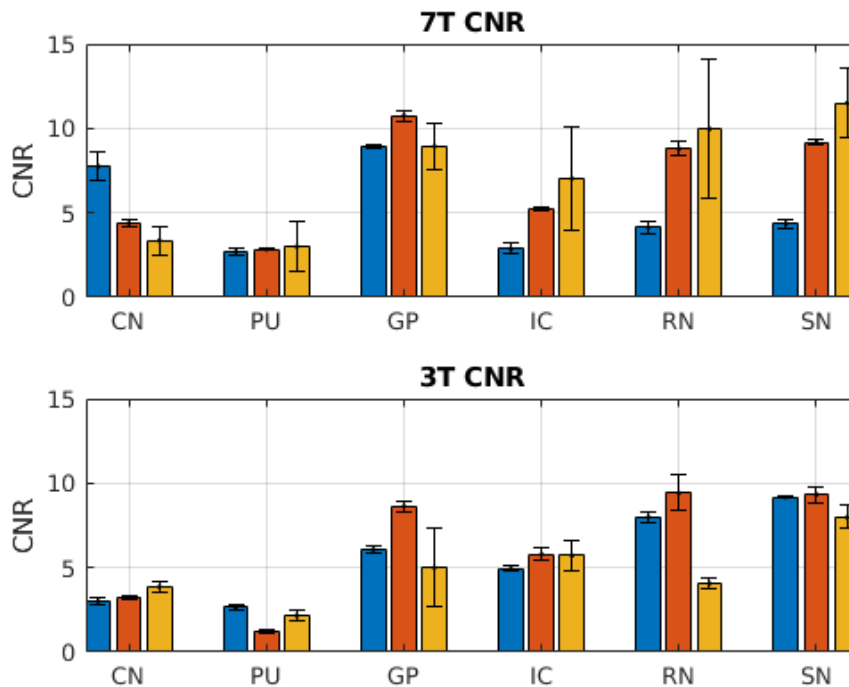
Figure 22: CNR values for each ROI at both 3 T and 7 T for EPI-QSM (blue), 2-D GRE-QSM (orange), and 3-D GRE-QSM (yellow).

7.3   Further Experimentation

7.3.1   Experiment 1: Time-averaging in Echo Planar Imaging

Twelve time repeats were taken at 3 T and 7 T and improvement in SNR was assessed qualitatively for one, three, six, and twelve repeats. Susceptibility maps for two sagittal slices at 3 T and 7 T are shown in Figure 23.

SNR was evaluated to determine if SNR gains from multiple measurements outweighed SNR losses from inter-measurement patient motion. SNR differences are especially evident in brain regions where susceptibility values are relatively homogenous. They include cerebral white matter (red detail boxes) and the pons of the brainstem (blue detail boxes).

At 3 T, SNR was highest for twelve time repeats and lowest for a single time repeat. Improvements were clear in both detailed regions at every increase of measurement number. At 7 T, SNR improved was clear between a single time point and three time repeats. However, SNR improvements for six and twelve time repeats is difficult to discern.

54

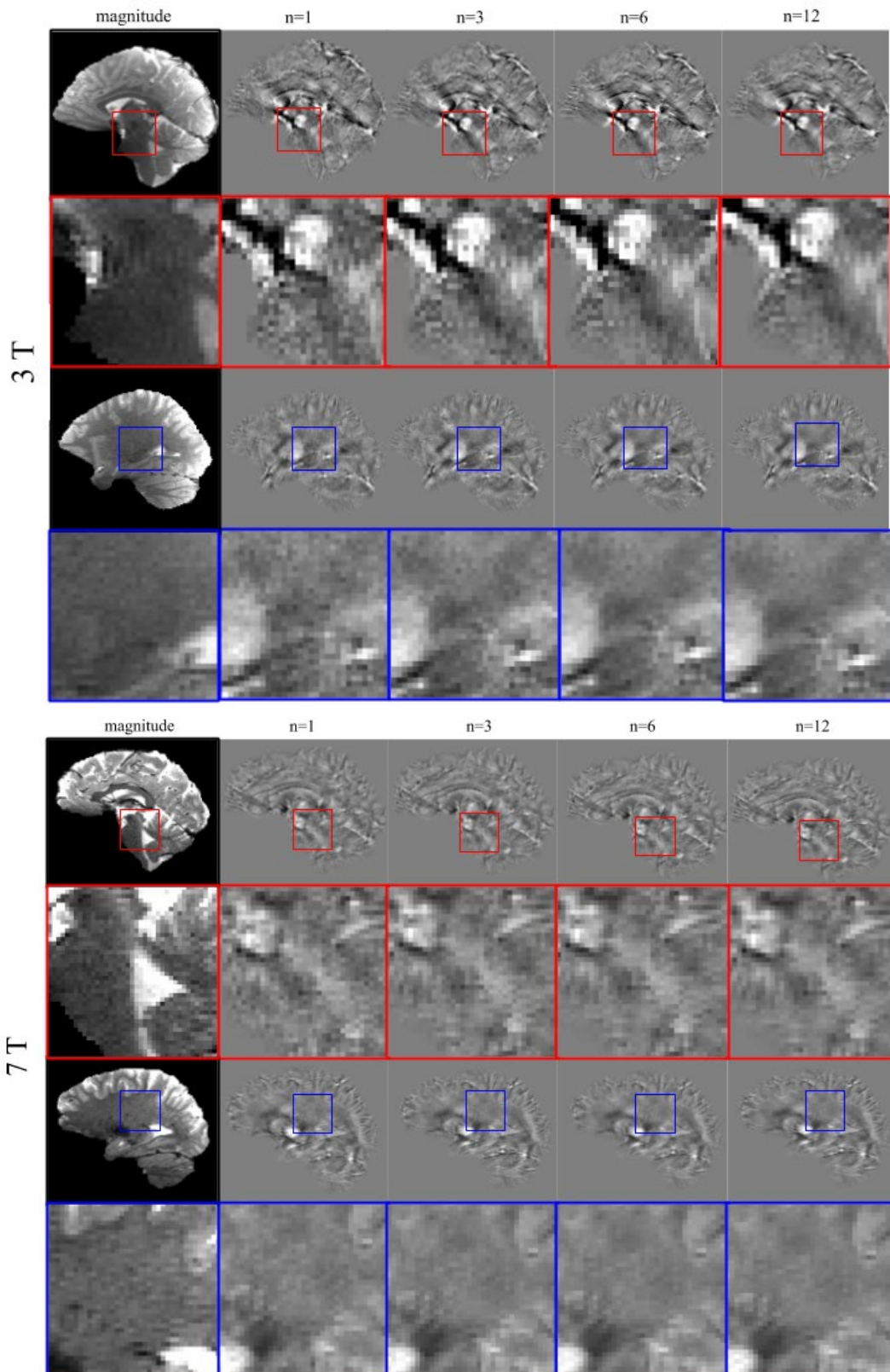**Figure 23: Susceptibility maps from a single EPI time point compared to susceptibility maps from multiple EPI repeats averaged together. Reduction in noise is most evident in regions of where susceptibility values should be relatively constant, especially in the pons of the brainstem (red boxes) and cerebral white matter (blue boxes). Left-most column contains a magnitude image for anatomical reference.**

7.3.2 Experiment 2: Echo-averaging in multi-echo Gradient Echo Imaging

Susceptibility maps were calculated for the first echo, second echo, and both echoes averaged together. Results are shown in Figure 24.

Masks were generated individually for each echo and affected the results. Masks at the first echo time were more conservative than masks at the second echo time. They included more voxels near the border of the brain.

Echo-averaged susceptibility maps had more consistent susceptibility values and fewer outliers of extreme susceptibility values than their single echo counterparts. In Row 1 Column 1 of Figure 24, a strong dipole shaped artifact is visible in the first echo QSM image, due to inclusion of background voxels. This strong dipole artifact is not visible in the second echo QSM image, confirmed by the difference map in Row 1 Column 1, and its strong influence is mediated in the final averaged QSM image.

Additional background signal is evident in the first echo image in Row 3 Column 1 of Figure 24, and its presence is reduced in the final averaged QSM image (Row 3 Column 4) by the exclusion of that region in the second echo image (Row 3 Column 2).
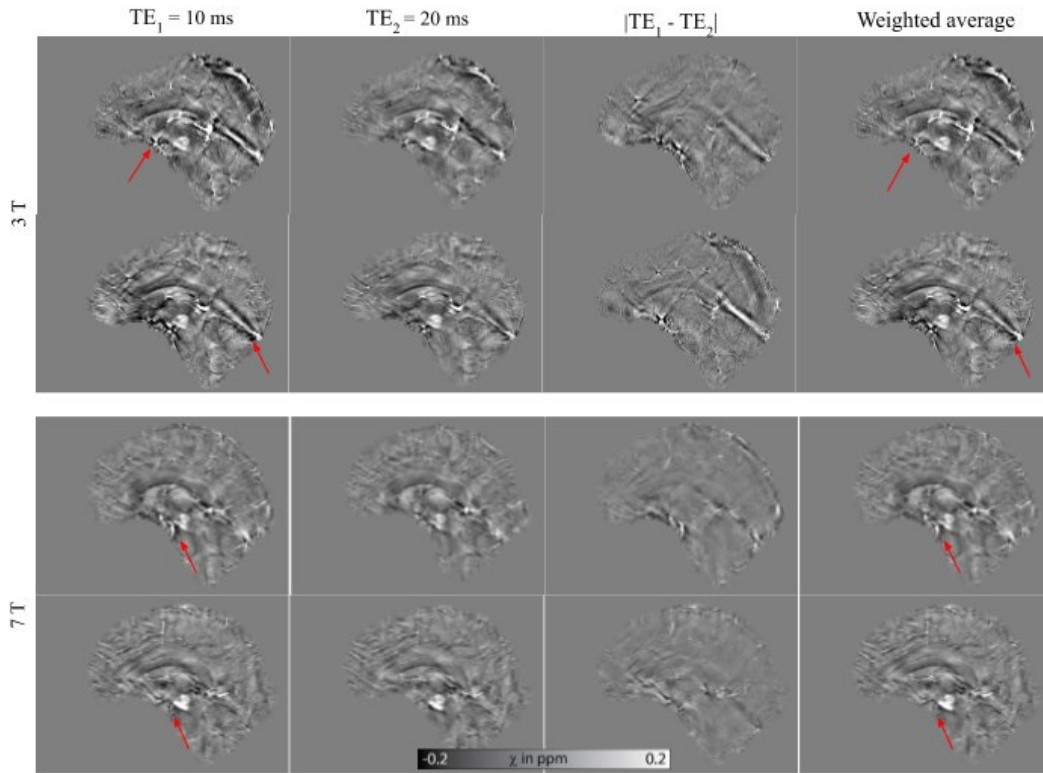

Figure 24: Susceptibility maps for 2-D GRE-QSM. Rows 1 and 2 show sagittal slices acquired at 3 T while rows 3 and 4 show slices acquired at 7 T. Difference maps in Column 3 are the absolute values of TE1-TE2 and the weighted-average in Column 4 is weighted according the GRE magnitude images. Susceptibility maps for the first echo showed more widely varying susceptibility values, shown in all four rows of Column 1 by red arrows. In all four cases, the range of susceptibility values was less in the corresponding second echo images. Images acquired at the second echo time may have had lower overall signal but showed better contrast for susceptibility values of gray and white matter.

7.3.3 Experiment 3: High Field vs Ultra-High Field Strength

Susceptibility maps at both high field and ultra-high field are shown in Figure 25. All subcortical and brainstem structures defined as ROIs can be identified from their surroundings for all sequence types at both field strengths.

Upon visual inspection, structures of interest including GP, RN, and SN all appear more paramagnetic and recognizable at 3 T than at 7 T. However, this did not correlate directly to higher CNR values.
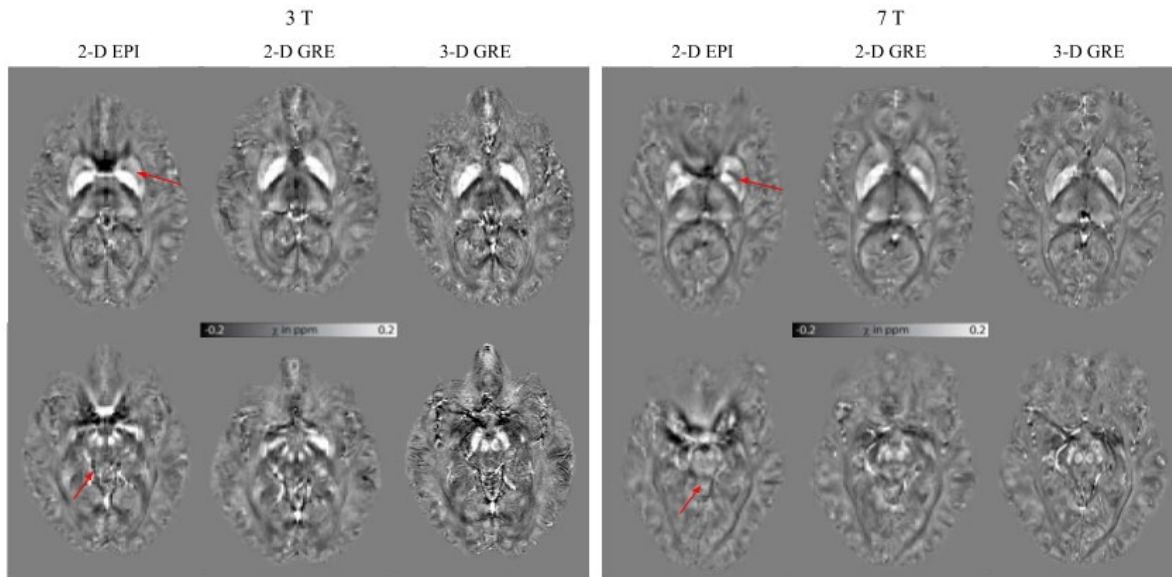

Figure 25: Susceptibility maps for all three sequences at both high and ultra-high field. EPI-QSM produced susceptibility maps with wider variability than 7 T (red arrows). Highest CNR was found in the gold standard 3-D GRE-QSM at 3 T, while 3-D GRE-QSM suffered from low CNR at 3 T.

Table 6 indicated the field strength at which a particular ROI had higher CNR. High field outperformed ultra-high field in terms of CNR only for 2-D EPI. For both types of GRE sequences, susceptibility maps with higher CNR were produced at ultra-high field.

Susceptibility values in EPI-QSM were twice as close to the gold standard on average at 3 T than at 7 T, while susceptibility values matched the gold standard slightly more closely at 7 T than 3 T for GRE-QSM, as seen in Table 4.

7.3.4 Experiment 4: Super-resolution Quantitative Susceptibility Mapping

Susceptibility maps are compared side-by-side to one of their matching, non-super-resolution volumes in Figure 26. Axial slices are shown to better highlight reduction in slice thickness of sagittally-acquired slices. Super-resolution volumes were made up of 125 slices. Slices in the edge regions of the super-resolution volumes, where susceptibility values are unreliable due to the nature of the dipole inversion calculation, remain far away from important brainstem structures because each slice is only 0.25 mm wide. Though the same number of slices were unreliable in the non-super-resolution volumes, they reach closer to important brainstem structures because each slice is 1.5 mm.

Super-resolution GRE-QSM images showed more detailed contours for RN and SN, including some detail of fibrous contours.

Super-resolution EPI-QSM images were more robust against signal dropout in deep brain regions and produced a more even signal profile. Both SN were not detectable in non-super-resolution EPI-QSM images, and there was significantly higher noise.
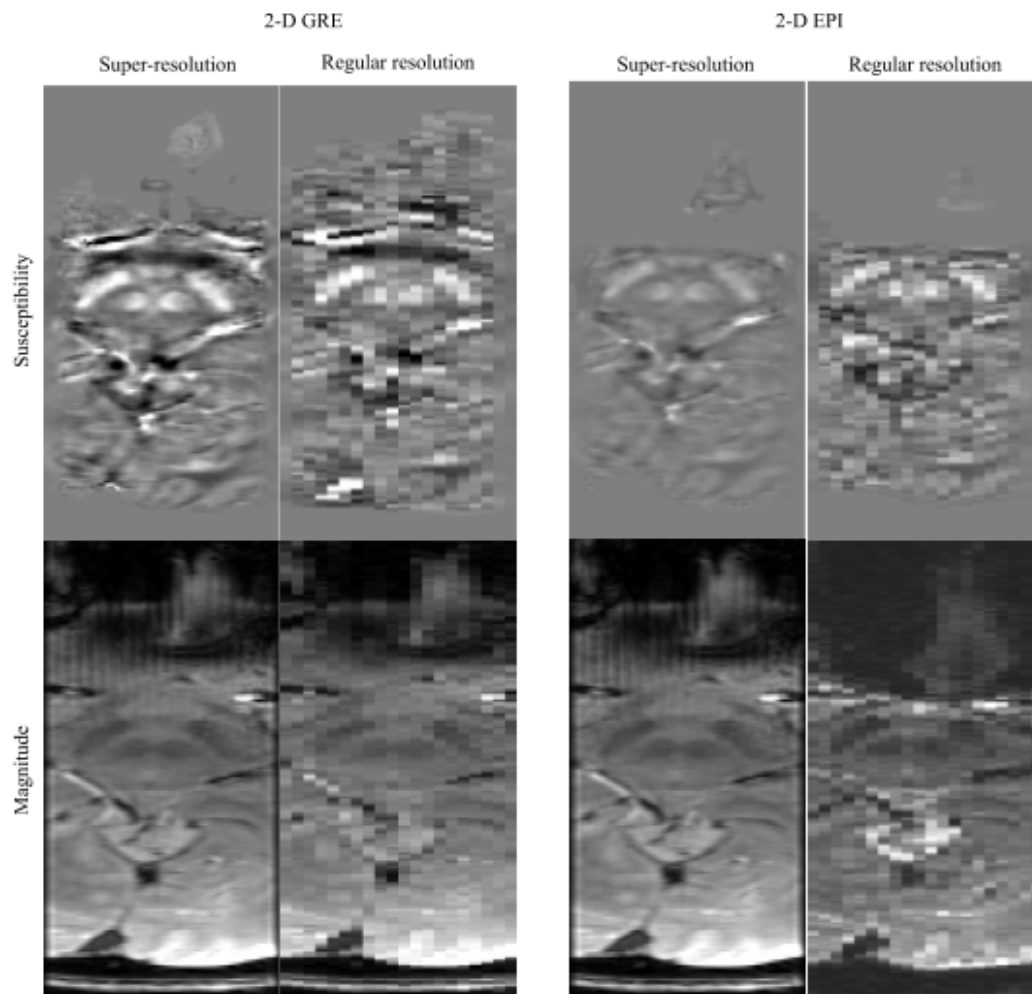
Figure 26: Super-resolution EPI-QSM and GRE-QSM with 0.25mm effective slice widths versus their matching QSM images with 1.5 mm slide width. Axial slices of the brainstem showing RN and SN are displayed to visualize the reduced slice width in the sagittal direction. Signal dropout heavily affected non-super-resolution EPI-QSM. Super-resolution EPI-QSM had more even signal across the brainstem volume and produced a QSM image with contrast around RN and SN. Though non-super-resolution GRE-QSM showed contrast around RN and SN, contours and fine structures are better visible in super-resolution GRE-QSM.

8 Discussion

The goal of this thesis was to develop QSM pipelines to generate the best possible susceptibility maps derived from 2-D EPI sequences, at both high and ultra-high field, as measured by agreement of susceptibility values with those derived from 2-D GRE and 3-D GRE sequences, and the possibility to visualize subcortical and brainstem nuclei.

QSM analysis of the brainstem at ultra-high field is well-documented, but is commonly carried using GRE images (43)(109)(16)(110). 3-D EPI sequences have also been used at ultra-high field for QSM (89)(111) but 2-D EPI-QSM at ultra-high field has not been widely explored. EPI-based sequences offer the possibility to dramatically reduce the measurement time or allow the generation of QSM from fMRI study data (i.e. with no additional acquisition time), but differences in the image characteristic of EPI compared to GRE – reduced SNR, distortion, signal dropout – mean that dedicated methods for EPI-QSM need to be explored. Algorithms for QSM steps - phase unwrapping, background field removal, and dipole inversion - were tested and compared in their effectiveness at identifying key brainstem structures. The feasibility of generating reliable susceptibility maps from 2-D EPI sequences was evaluated.

Masking – removal of non-brain parts of the image – allows susceptibility sources outside the image from those within the image to be distinguished and is an essential step in solving the QSM problem. BET masking from FSL (112) is the most widely used masking technique for QSM, being the default for the MEDI toolbox (104), STI Suite (103), and Sepia toolbox (105). These QSM packages are tailored towards GRE-QSM, however. In QSM based on single-shot EPI measurements, Sun and Wilman used BET masking (88), but noted issues related to distortions at the border of air-tissue interfaces. When calculating susceptibility maps directly from standard fMRI measurements, they used SPM segmentation (23), because it is a part of a wider SPM package developed specifically for fMRI. In another study on EPI-based QSM, Bachratá used BET masking in QSM analysis of 2-D single shot EPI images but noted that signal dropout and distortions prevented effecting masking in frontal regions (113). In this study, the most effective brain mask was found to be a composite mask generated from two different brain-masking approaches - BET and SPM.

The BET-only and SPM-only masks generated in this study yielded inaccurate susceptibility maps for 2-D EPI images. The composite BET SPM mask we describe was the only feasible option and justified the added complexity of creating it. This solution improved on masking accuracy, specifically in frontal regions and borders between paranasal sinuses and brainstem, which allowed more accurate susceptibility values to be calculated.

Laplacian-based phase unwrapping proved to be the most reliable phase unwrapping algorithm as it accurately removed all wraps and preserved tissue phase contrast in the brain volume. Compared to phase unwrapping of 2-D EPI phase maps at 3 T by Wei et al. (107), Laplacian-based phase unwrapping produced total field maps of similar quality in this study at both 3 T and 7 T. Total field maps for both EPI and GRE at 7 T agreed with those produced by Deistung et al. for GRE-QSM at 7 T (43).

VSHARP background field removal produced the best local field maps, based on contrast within the brain volume and lack of blooming artifacts. VSHARP, developed by Wu et al. in 2012 (68), was designed to improve behavior in border regions by using a variable spherical kernel size. VSHARP did indeed produce fewer artifacts near the border than iHARPERELLA and LBV, especially for GRE images. Agreeing with Wei et al. (107), combined 2-D + 3-D VSHARP background field removal produced better local field maps for EPI images than 2-D VSHARP alone at 3 T. This study expanded on Wei et al.'s strategy by testing it at 7 T, and

found effectiveness at ultra-high field. Differences between local field maps were largely confined to border regions, while deep brain regions were roughly equivalent. This is in line with a comparative analysis carried out by Schweser et al., who determined that background field algorithms produced only minor differences that were primarily in cortical region of the brain (114).

Susceptibility maps varied widely between dipole inversion algorithms, with MEDI+0 producing a heavily streaked map and FANSI producing a heavily smoothed map, however, a wide range of normalization parameters was not explored. Out of the algorithms tested, STAR-QSM produced the most accurate susceptibility maps. MEDI+0 may have produced a worse susceptibility map for EPI than GRE because it makes assumptions based on anatomical information in the magnitude image, which is distorted in EPI. Deep learning techniques have been proposed to solve the ill-posed inverse problem for QSM, such as DeepQSM (115) and QSMnet (116), indicating that susceptibility mapping for EPI is likely to continue to improve.

Compared to 2-D EPI-QSM at ultra-high field produced by Bachratá (113) using a single-step QSM approach called total generalized variation, 2-D EPI-QSM in this study had more accurate susceptibility values. This study's susceptibility maps had higher CNR, less blurring, and susceptibilities closer to their 3-D GRE counterparts.

QSM maps based on 2-D EPI showed highest agreements of susceptibility values with 3-D GRE QSMs for the putamen, and lowest agreement for the caudate nuclei. Susceptibilities were more consistent between 2-D EPI and the gold standard at 3 T than at 7 T. There was no trend towards consistently over- or underestimating susceptibility in 2-D EPI-QSM. Wide ranges of susceptibility values limit QSM results' usefulness in quantifying susceptibility and drawing conclusions from those values, especially when differing scan parameters and sequences are used.

Patterns of susceptibility for brainstem and subcortical nuclei were in line with previous studies. The ranking of susceptibilities found in this study in decreasing order is SN, GP, RN, PU, CN, IC, which matches the ranking of Sun and Wilman's 2-D EPI analysis at 4.7 T (23), although susceptibility values themselves were up to 50% larger or smaller than Sun and Wilman's.

More importantly for the feasibility of using EPI-QSM to localize small structures, CNR values indicated that all six brainstem and subcortical structures were distinguishable from their surroundings at both field strengths. For 3 ROIs at 7 T, CNR values for EPI-QSM were less than half of the gold standard values. Average CNRs for all structures in EPI-QSM were closer to the gold standard at 3 T, indicating that high field EPI-QSM may actually be better suited to applications for brainstem structure localization than ultra-high field. This contradicts findings of Straub et al. (109), who compared CNRs of brainstem structures at 3 T and 7 T and found a two- to three-fold increase in CNR at ultra-high field. Repeating the procedure used in this study on several healthy subjects is required before drawing further conclusions about CNR and field strength.

Agreeing with results from Sun and Wilman (88), weighted-averaging of individual EPI-QSM susceptibility maps from multiple time repeats showed increased SNR. SNR at high field increased at each successive level of time repeats: 3, 6, and 12. At ultra-high field, SNR increased from a single time point to 3 repeats but was not discernable for more time repeats above 3. This indicates that measurement time and computation time can be saved at ultra-high field by only acquiring three EPI repeats. A typical fMRI protocol, which uses 2-D EPI, starts with three dummy excitations before measurement begins in order to ensure quasi-equilibrium

in longitudinal magnetization. These dummy excitations could be replaced by acquisitions for QSM, allowing high resolution QSM to be generated without any additional scan time.

Wu et al. (31) showed improved SNR in GRE-QSM by combining susceptibility maps from five echo times, ranging between 10 ms and 50 ms. Our study showed similar results, with weighted-averaging of individual GRE-QSM susceptibility maps from each echo in a multi-echo acquisition showing more consistent susceptibility values. Susceptibility maps from the second echo were generally more reliable across the entire brain volume. That the second echo time was 20 ms, closer to the average T_2^* relaxation time of gray and white matter, roughly 30 ms at 7 T (9), could have contributed to this result. However, the first echo would provide more signal for tissues with strong susceptibilities that may have shorter T_2^* relaxation times. To get a susceptibility map for a wide range of tissues in the brain, weighted-average multi-echo GRE-QSM is more effective than single echo GRE-QSM.

There was significant variation in susceptibility values between field strengths, indicating that while the QSM pipeline accurately shows trends in susceptibility, it is not yet effective at delivering a reproducible result with sufficient precision. The percent differences between susceptibility values in EPI-QSM and 3-D GRE-QSM were half as large at 3 T than at 7 T. Greater geometric distortions at 7 T could have caused the susceptibility values to vary more from their gold standards at ultra-high field strength. Zwanenburg et al. showed long echo train lengths in EPI sequences at 7 T having a strong effect on geometric distortion (117) and Stäb et al. cite the increased effect of distortion at ultra-high field strength (111).

Preliminary QSM processing of super-resolution EPI images developed by Ehrmann et al. demonstrate that susceptibility mapping of super-resolution reconstructed phase images is possible (91). One key improvement in super-resolution QSM over conventional QSM stems from the super-resolution volume's higher number of, and thinner slices padding the edge of the volume. A fixed number of edge slices are unreliable in susceptibility maps due to the dipole inversion calculation and thinner super-resolution slices ensure that the unreliable slices are distant from brainstem structures of interest.

To build more robust data for statistical analysis of the ROIs, the imaging protocol could be carried out on several patients at both field strengths. This would potentially reduce variance in susceptibility values and allow more powerful conclusions to be drawn about the accuracy of susceptibility maps across sequence types.

EPI-QSM may be limited in comparison to GRE-QSM because optimum phase contrast occurs when the TE is roughly equal to the tissue's effective transverse relaxation time, T_2^*. Therefore, multi-echo GRE allows more flexibility in choosing contrast that is optimal in a brain volume with widely varying T_2^* relaxation times . In this study, TEs for EPI sequences were 25 ms and 29 ms, which could produce lower phase contrast in brain regions with shorter T_2^* relaxation.

Several future improvements could be made to further develop this work. Using an algorithm that compensates for geometric distortion and related signal loss in EPI images, such as FUGUE from FSL (118), could create more reliable brain masks and potentially more reliable susceptibility maps. A motion correction tool such as MCFLIRT form FSL (119) could improve susceptibility map consistency across many time points, paving the way for fQSM analysis. Brains could be registered to a standard space for more direct comparison of ROIs across subjects and field strengths. A super-resolution algorithm could be improved to increase inter-slice continuity. To reduce acquisition time even more, the minimal number of sagittal slices required to produce reliable QSM results for the brainstem region could be explored.

Results for EPI-QSM are promising enough to continue pursuing EPI-QSM as a means to study the brainstem. When further considerations of EPI imaging relevant to the brainstem are taken into account, such as physiological noise correction and dynamic distortion correction, this MR method has potential for future clinical applications.

9   Conclusion

A QSM pipeline for the localization of brainstem and subcortical nuclei from 2-D EPI images was developed. Laplacian-based phase unwrapping, a combination of BET and SPM brain masking, VSHARP background field removal, and STAR-QSM dipole inversion led to the most reliable QSM results.

Susceptibility maps generated by 2-D EPI phase images were shown to provide sufficient CNR to detect all six subcortical and brainstem structures analyzed, indicating promise for EPI-QSM for localization of brainstem nuclei in neurosurgical applications such as preoperative planning for DBS. However, measured susceptibility values varied too widely from literature values to be considered reliable for drawing quantitative conclusions.

Averaging multi-echo GRE susceptibility maps better reflected the magnetic susceptibility variation across tissues in the whole head volume than susceptibility maps based on a single echo. SNR improved in EPI-QSM when averaging susceptibility maps from multiple time repeats. Susceptibility values from EPI-QSM matched gold standard values more closely at 3 T than 7 T. Future directions for this research include further measurements in vivo to examine the reproducibility of susceptibility maps and performing QSM on super-resolution reconstructions of EPI phase data to further delineate small, complex brainstem structures.

10 References

1. Dusek P, Roos PM, Litwin T, Schneider SA, Flaten TP, Aaseth J. The neurotoxicity of iron, copper and manganese in Parkinson's and Wilson's diseases. J Trace Elem Med Biol Organ Soc Miner Trace Elem GMS. 2015;31:193–203.

2. Limousin P, Krack P, Pollak P, Benazzouz A, Ardouin C, Hoffmann D, Benabid AL. Electrical stimulation of the subthalamic nucleus in advanced Parkinson's disease. N Engl J Med. 1998 Oct 15;339(16):1105–11.

3. Follett KA, Weaver FM, Stern M, Hur K, Harris CL, Luo P, Marks WJ, Rothlind J, Sagher O, Moy C, Pahwa R, Burchiel K, Hogarth P, Lai EC, Duda JE, Holloway K, Samii A, Horn S, Bronstein JM, Stoner G, Starr PA, Simpson R, Baltuch G, De Salles A, Huang GD, Reda DJ. Pallidal versus subthalamic deep-brain stimulation for Parkinson's disease. N Engl J Med. 2010 Jun 3;362(22):2077–91.

4. Abosch A, Timmermann L, Bartley S, Rietkerk HG, Whiting D, Connolly PJ, Lanctin D, Hariz MI. An international survey of deep brain stimulation procedural steps. Stereotact Funct Neurosurg. 2013;91(1):1–11.

5. VanSickle D, Volk V, Freeman P, Henry J, Baldwin M, Fitzpatrick CK. Electrode Placement Accuracy in Robot-Assisted Asleep Deep Brain Stimulation. Ann Biomed Eng. 2019 May;47(5):1212–22.

6. Schweser F, Deistung A, Lehr BW, Reichenbach JR. Quantitative imaging of intrinsic magnetic tissue properties using MRI signal phase: an approach to in vivo brain iron metabolism? NeuroImage. 2011 Feb 14;54(4):2789–807.

7. de Rochefort L, Liu T, Kressler B, Liu J, Spincemaille P, Lebon V, Wu J, Wang Y. Quantitative susceptibility map reconstruction from MR phase data using bayesian regularization: validation and application to brain imaging. Magn Reson Med. 2010 Jan;63(1):194–206.

8. Shmueli K, de Zwart JA, van Gelderen P, Li T-Q, Dodd SJ, Duyn JH. Magnetic susceptibility mapping of brain tissue in vivo using MRI phase data. Magn Reson Med. 2009 Dec;62(6):1510–22.

9. Duyn JH, van Gelderen P, Li T-Q, de Zwart JA, Koretsky AP, Fukunaga M. High-field MRI of brain cortical substructure based on signal phase. Proc Natl Acad Sci U S A. 2007 Jul 10;104(28):11796–801.

10. Chen W, Zhu W, Kovanlikaya I, Kovanlikaya A, Liu T, Wang S, Salustri C, Wang Y. Intracranial calcifications and hemorrhages: characterization with quantitative susceptibility mapping. Radiology. 2014 Feb;270(2):496–505.

11. Schweser F, Deistung A, Lehr BW, Reichenbach JR. Differentiation between diamagnetic and paramagnetic cerebral lesions based on magnetic susceptibility mapping. Med Phys. 2010 Oct;37(10):5165–78.

12. Bilgic B, Pfefferbaum A, Rohlfing T, Sullivan EV, Adalsteinsson E. MRI estimates of brain iron concentration in normal aging using quantitative susceptibility mapping. NeuroImage. 2012 Feb 1;59(3):2625–35.

13. Haacke EM, Cheng NYC, House MJ, Liu Q, Neelavalli J, Ogg RJ, Khan A, Ayaz M, Kirsch W, Obenaus A. Imaging iron stores in the brain using magnetic resonance imaging. Magn Reson Imaging. 2005 Jan;23(1):1–25.

14. Sun H, Walsh AJ, Lebel RM, Blevins G, Catz I, Lu J-Q, Johnson ES, Emery DJ, Warren KG, Wilman AH. Validation of quantitative susceptibility mapping with Perls' iron staining for subcortical gray matter. NeuroImage. 2015 Jan 15;105:486–92.

15. Langkammer C, Krebs N, Goessler W, Scheurer E, Ebner F, Yen K, Fazekas F, Ropele S. Quantitative MR imaging of brain iron: a postmortem validation study. Radiology. 2010 Nov;257(2):455–62.

16. Deistung A, Schäfer A, Schweser F, Biedermann U, Turner R, Reichenbach JR. Toward in vivo histology: a comparison of quantitative susceptibility mapping (QSM) with magnitude-, phase-, and R2*-imaging at ultra-high magnetic field strength. NeuroImage. 2013 Jan 15;65:299–314.

17. Lotfipour AK, Wharton S, Schwarz ST, Gontu V, Schäfer A, Peters AM, Bowtell RW, Auer DP, Gowland PA, Bajaj NPS. High resolution magnetic susceptibility mapping of the substantia nigra in Parkinson's disease. J Magn Reson Imaging JMRI. 2012 Jan;35(1):48–55.

18. Langkammer C, Liu T, Khalil M, Enzinger C, Jehna M, Fuchs S, Fazekas F, Wang Y, Ropele S. Quantitative susceptibility mapping in multiple sclerosis. Radiology. 2013 May;267(2):551–9.

19. Berg D, Youdim MBH. Role of iron in neurodegenerative disorders. Top Magn Reson Imaging TMRI. 2006 Feb;17(1):5–17.

20. Deistung A, Schweser F, Reichenbach JR. Overview of quantitative susceptibility mapping. NMR Biomed. 2017 Apr;30(4).

21. Sati P, Thomasson DM, Li N, Pham DL, Biassou NM, Reich DS, Butman JA. Rapid, high-resolution, whole-brain, susceptibility-based MRI of multiple sclerosis. Mult Scler Houndmills Basingstoke Engl. 2014 Oct;20(11):1464–70.

22. Mansfield P. Real-time echo-planar imaging by NMR. Br Med Bull. 1984 Apr;40(2):187–90.

23. Sun H, Seres P, Wilman AH. Structural and functional quantitative susceptibility mapping from standard fMRI studies. NMR Biomed. 2017 Apr;30(4).

24. Xu Y, Haacke EM. An iterative reconstruction technique for geometric distortion-corrected segmented echo-planar imaging. Magn Reson Imaging. 2008 Dec;26(10):1406–14.

25. Jezzard P, Balaban RS. Correction for geometric distortion in echo planar images from B0 field variations. Magn Reson Med. 1995 Jul;34(1):65–73.

26. Brown RW, Cheng Y-CN, Haacke EM, Thompson MR, Venkatesan R. Magnetic Resonance Imaging: Physical Principles and Sequence Design. 2nd ed. Wiley Blackwell; 2014.

27. Miller K. MRI Image Formation [Internet]. FMRIB Physics Group, University of Oxford; Available from: users.fmrib.ox.ac.uk/~karla/teaching/image_formation.ppt

28. Magnetic Resonance Imaging: Image Reconstruction [Internet]. Oncology Medical Physics. Available from: https://oncologymedicalphysics.com/magnetic-resonance-imaging/

29. IMAIOS. e-MRI: Gradient echo sequence [Internet]. e-MRI. Available from: https://www.imaios.com/en/e-Courses/e-MRI/MRI-Sequences/gradient-echo

30. Gaillard F. MRI Physics (diagrams) [Internet]. Radiopaedia. Available from: https://radiopaedia.org/cases/mri-physics-diagrams-1?lang=us

31. Wu B, Li W, Avram AV, Gho S-M, Liu C. Fast and tissue-optimized mapping of magnetic susceptibility and T2* with multi-echo and multi-shot spirals. NeuroImage. 2012 Jan 2;59(1):297–305.

32. Elster AD. Echo-Planar Imaging (EPI) [Internet]. Questions and Answers in MRI. Available from: http://www.mriquestions.com/echo-planar-imaging.html

33. Poustchi-Amin M, Mirowitz SA, Brown JJ, McKinstry RC, Li T. Principles and applications of echo-planar imaging: a review for the general radiologist. Radiogr Rev Publ Radiol Soc N Am Inc. 2001 Jun;21(3):767–79.

34. Deshmane A, Gulani V, Griswold MA, Seiberlich N. Parallel MR imaging. J Magn Reson Imaging JMRI. 2012 Jul;36(1):55–72.

35. Fellner C, Doenitz C, Finkenzeller T, Jung EM, Rennert J, Schlaier J. Improving the spatial accuracy in functional magnetic resonance imaging (fMRI) based on the blood

oxygenation level dependent (BOLD) effect: benefits from parallel imaging and a 32-channel head array coil at 1.5 Tesla. Clin Hemorheol Microcirc. 2009;43(1–2):71–82.

36. Boujraf S, Summers P, Belahsen F, Prüssmann K, Kollias S. Ultrafast bold fMRI using single-shot spin-echo echo planar imaging. J Med Phys. 2009 Jan;34(1):37–42.

37. Griswold MA, Jakob PM, Heidemann RM, Nittka M, Jellus V, Wang J, Kiefer B, Haase A. Generalized autocalibrating partially parallel acquisitions (GRAPPA). Magn Reson Med. 2002 Jun;47(6):1202–10.

38. Haacke EM, Xu Y, Cheng Y-CN, Reichenbach JR. Susceptibility weighted imaging (SWI). Magn Reson Med. 2004 Sep;52(3):612–8.

39. Roemer PB, Edelstein WA, Hayes CE, Souza SP, Mueller OM. The NMR phased array. Magn Reson Med. 1990 Nov;16(2):192–225.

40. Nowogrodzki A. The world's strongest MRI machines are pushing human imaging to new limits. Nature. 2018;563(7729):24–6.

41. Trattnig S, Springer E, Bogner W, Hangel G, Strasser B, Dymerska B, Cardoso PL, Robinson SD. Key clinical benefits of neuroimaging at 7T. NeuroImage. 2018;168:477–89.

42. Springer E, Dymerska B, Cardoso PL, Robinson SD, Weisstanner C, Wiest R, Schmitt B, Trattnig S. Comparison of Routine Brain Imaging at 3 T and 7 T. Invest Radiol. 2016;51(8):469–82.

43. Deistung A, Schäfer A, Schweser F, Biedermann U, Güllmar D, Trampel R, Turner R, Reichenbach JR. High-Resolution MR Imaging of the Human Brainstem In vivo at 7 Tesla. Front Hum Neurosci. 2013;7:710.

44. Liu C, Li W, Tong KA, Yeom KW, Kuzminski S. Susceptibility-weighted imaging and quantitative susceptibility mapping in the brain. J Magn Reson Imaging JMRI. 2015 Jul;42(1):23–41.

45. Li W, Liu C, Duong TQ, van Zijl PCM, Li X. Susceptibility tensor imaging (STI) of the brain. NMR Biomed. 2017 Apr;30(4).

46. Wen J, Cross AH, Yablonskiy DA. On the role of physiological fluctuations in quantitative gradient echo MRI: implications for GEPCI, QSM, and SWI. Magn Reson Med. 2015 Jan;73(1):195–203.

47. Wang Y, Spincemaille P, Liu Z, Dimov A, Deh K, Li J, Zhang Y, Yao Y, Gillen KM, Wilman AH, Gupta A, Tsiouris AJ, Kovanlikaya I, Chiang GC-Y, Weinsaft JW, Tanenbaum L, Chen W, Zhu W, Chang S, Lou M, Kopell BH, Kaplitt MG, Devos D, Hirai T, Huang X, Korogi Y, Shtilbans A, Jahng G-H, Pelletier D, Gauthier SA, Pitt D, Bush AI, Brittenham GM, Prince MR. Clinical quantitative susceptibility mapping (QSM): Biometal imaging and its emerging roles in patient care. J Magn Reson Imaging JMRI. 2017;46(4):951–71.

48. Bowtell RW. Magnetic Susceptibility of Biological Tissues. ESMRMB Lectures on MR 2014: Susceptibility Weighted Imaging and Quantitative Mapping, Graz, Austria 2014.

49. Robinson SD, Bredies K, Khabipova D, Dymerska B, Marques JP, Schweser F. An illustrated comparison of processing methods for MR phase imaging and QSM: combining array coil signals and phase unwrapping. NMR Biomed. 2017 Apr;30(4).

50. Eckstein K, Dymerska B, Bachratá B, Bogner W, Poljanc K, Trattnig S, Robinson SD. Computationally Efficient Combination of Multi-channel Phase Data From Multi-echo Acquisitions (ASPIRE). Magn Reson Med. 2018;79(6):2996–3006.

51. Xiang QS. Temporal phase unwrapping for CINE velocity imaging. J Magn Reson Imaging JMRI. 1995 Oct;5(5):529–34.

52. Robinson S, Schödl H, Trattnig S. A method for unwrapping highly wrapped multi-echo phase images at very high field: UMPIRE. Magn Reson Med. 2014 Jul;72(1):80–92.

53. Bioucas-Dias JM, Valadão G. Phase unwrapping via graph cuts. IEEE Trans Image Process Publ IEEE Signal Process Soc. 2007 Mar;16(3):698–709.

54. Abdul-Rahman HS, Gdeisat MA, Burton DR, Lalor MJ, Lilley F, Moore CJ. Fast and robust three-dimensional best path phase unwrapping algorithm. Appl Opt. 2007 Sep 10;46(26):6623–35.

55. Witoszynskyj S, Rauscher A, Reichenbach JR, Barth M. Phase unwrapping of MR images using Phi UN--a fast and robust region growing algorithm. Med Image Anal. 2009 Apr;13(2):257–68.

56. Karsa A, Shmueli K. SEGUE: A Speedy rEgion-Growing Algorithm for Unwrapping Estimated Phase. IEEE Trans Med Imaging. 2019;38(6):1347–57.

57. Schofield MA, Zhu Y. Fast phase unwrapping algorithm for interferometric applications. Opt Lett. 2003 Jul 15;28(14):1194–6.

58. Bagher-Ebadian H, Jiang Q, Ewing JR. A modified Fourier-based phase unwrapping algorithm with an application to MRI venography. J Magn Reson Imaging JMRI. 2008 Mar;27(3):649–52.

59. Neelavalli J, Cheng Y-CN, Jiang J, Haacke EM. Removing background phase variations in susceptibility-weighted imaging using a fast, forward-field calculation. J Magn Reson Imaging JMRI. 2009 Apr;29(4):937–48.

60. Smith SM. Fast robust automated brain extraction. Hum Brain Mapp. 2002 Nov;17(3):143–55.

61. Jenkinson M, Beckmann CF, Behrens TEJ, Woolrich MW, Smith SM. FSL. NeuroImage. 2012 Aug 15;62(2):782–90.

62. SPM12 [Internet]. Available from: https://www.fil.ion.ucl.ac.uk/spm/

63. Wen Y, Zhou D, Liu T, Spincemaille P, Wang Y. An iterative spherical mean value method for background field removal in MRI. Magn Reson Med. 2014 Oct;72(4):1065–71.

64. Wang Y, Yu Y, Li D, Bae KT, Brown JJ, Lin W, Haacke EM. Artery and vein separation using susceptibility-dependent phase in contrast-enhanced MRA. J Magn Reson Imaging JMRI. 2000 Nov;12(5):661–70.

65. Haacke EM, Ayaz M, Khan A, Manova ES, Krishnamurthy B, Gollapalli L, Ciulla C, Kim I, Petersen F, Kirsch W. Establishing a baseline phase behavior in magnetic resonance imaging to determine normal vs. abnormal iron content in the brain. J Magn Reson Imaging JMRI. 2007 Aug;26(2):256–64.

66. Liu T, Khalidov I, de Rochefort L, Spincemaille P, Liu J, Tsiouris AJ, Wang Y. A novel background field removal method for MRI using projection onto dipole fields (PDF). NMR Biomed. 2011 Nov;24(9):1129–36.

67. Li L, Leigh JS. High-precision mapping of the magnetic field utilizing the harmonic function mean value property. J Magn Reson San Diego Calif 1997. 2001 Feb;148(2):442–8.

68. Wu B, Li W, Guidon A, Liu C. Whole brain susceptibility mapping using compressed sensing. Magn Reson Med. 2012 Jan;67(1):137–47.

69. Zhou D, Liu T, Spincemaille P, Wang Y. Background field removal by solving the Laplacian boundary value problem. NMR Biomed. 2014 Mar;27(3):312–9.

70. Li W, Avram AV, Wu B, Xiao X, Liu C. Integrated Laplacian-based phase unwrapping and background phase removal for quantitative susceptibility mapping. NMR Biomed. 2014 Feb;27(2):219–27.

71. Bredies K. The Inverse Problem. ESMRMB Lectures on MR 2014: Susceptibility Weighted Imaging and Quantitative Mapping, Graz, Austria. 2014.

72. Zhang S, Liu Z, Nguyen TD, Yao Y, Gillen KM, Spincemaille P, Kovanlikaya I, Gupta A, Wang Y. Clinical feasibility of brain quantitative susceptibility mapping. Magn Reson Imaging. 2019;60:44–51.

73. Liu T, Spincemaille P, de Rochefort L, Kressler B, Wang Y. Calculation of susceptibility through multiple orientation sampling (COSMOS): a method for conditioning the inverse problem from measured magnetic field map to susceptibility source image in MRI. Magn Reson Med. 2009 Jan;61(1):196–204.

74. Wharton S, Schäfer A, Bowtell R. Susceptibility mapping in the human brain using threshold-based k-space division. Magn Reson Med. 2010 May;63(5):1292–304.

75. Liu J, Liu T, de Rochefort L, Ledoux J, Khalidov I, Chen W, Tsiouris AJ, Wisnieff C, Spincemaille P, Prince MR, Wang Y. Morphology enabled dipole inversion for quantitative susceptibility mapping using structural consistency between the magnitude image and the susceptibility map. NeuroImage. 2012 Feb 1;59(3):2560–8.

76. Li W, Wang N, Yu F, Han H, Cao W, Romero R, Tantiwongkosi B, Duong TQ, Liu C. A method for estimating and removing streaking artifacts in quantitative susceptibility mapping. NeuroImage. 2015 Mar;108:111–22.

77. Wei H, Dibb R, Zhou Y, Sun Y, Xu J, Wang N, Liu C. Streaking artifact reduction for quantitative susceptibility mapping of sources with large dynamic range. NMR Biomed. 2015 Oct;28(10):1294–303.

78. Bilgic B, Fan AP, Polimeni JR, Cauley SF, Bianciardi M, Adalsteinsson E, Wald LL, Setsompop K. Fast quantitative susceptibility mapping with L1-regularization and automatic parameter selection. Magn Reson Med. 2014 Nov;72(5):1444–59.

79. Mahdi K, Wlodarczky W, Lange T, Scholz R, Jordan A, Wust P. Quantitative mapping of magnetic fluid distributions by means of MR susceptometry. In: Proc ISMRM Annual Meeting. 2001.

80. Haacke EM, Liu S, Buch S, Zheng W, Wu D, Ye Y. Quantitative susceptibility mapping: current status and future directions. Magn Reson Imaging. 2015 Jan;33(1):1–25.

81. Chen W, Gauthier SA, Gupta A, Comunale J, Liu T, Wang S, Pei M, Pitt D, Wang Y Quantitative susceptibility mapping of multiple sclerosis lesions at various ages. Radiology. 2014 Apr;271(1):183–92.

82. Straub S, Laun FB, Emmerich J, Jobke B, Hauswald H, Katayama S, Herfarth K, Schlemmer H-P, Ladd ME, Ziener CH, Bonekamp D, Röthke MC. Potential of quantitative susceptibility mapping for detection of prostatic calcifications. J Magn Reson Imaging JMRI. 2017;45(3):889–98.

83. Acosta-Cabronero J, Williams GB, Cardenas-Blanco A, Arnold RJ, Lupson V, Nestor PJ. In vivo quantitative susceptibility mapping (QSM) in Alzheimer's disease. PloS One. 2013;8(11):e81093.

84. van Bergen JMG, Hua J, Unschuld PG, Lim IaL, Jones CK, Margolis RL, Ross CA, van Zijl PCM, Li X. Quantitative Susceptibility Mapping Suggests Altered Brain Iron in Premanifest Huntington Disease. AJNR Am J Neuroradiol. 2016 May;37(5):789–96.

85. Schweitzer AD, Liu T, Gupta A, Zheng K, Seedial S, Shtilbans A, Shahbazi M, Lange D, Wang Y, Tsiouris AJ. Quantitative susceptibility mapping of the motor cortex in amyotrophic lateral sclerosis and primary lateral sclerosis. AJR Am J Roentgenol. 2015 May;204(5):1086–92.

86. Liu T, Eskreis-Winkler S, Schweitzer AD, Chen W, Kaplitt MG, Tsiouris AJ, Wang Y. Improved subthalamic nucleus depiction with quantitative susceptibility mapping. Radiology. 2013 Oct;269(1):216–23.

87. Ashkan K, Blomstedt P, Zrinzo L, Tisch S, Yousry T, Limousin-Dowsey P, Hariz MI. Variability of the subthalamic nucleus: the case for direct MRI guided targeting. Br J Neurosurg. 2007 Apr;21(2):197–200.

88. Sun H, Wilman AH. Quantitative susceptibility mapping using single-shot echo-planar imaging. Magn Reson Med. 2015 May;73(5):1932–8.

89. Balla DZ, Sanchez-Panchuelo RM, Wharton SJ, Hagberg GE, Scheffler K, Francis ST, Bowtell R. Functional quantitative susceptibility mapping (fQSM). NeuroImage. 2014 Oct 15;100:112–24.

90. Greenspan H, Oz G, Kiryati N, Peled S. MRI inter-slice reconstruction using super-resolution. Magn Reson Imaging. 2002 Jun;20(5):437–46.

91. Ehrmann A, Bachratá B, Eckstein K, Bancelin D, Cardoso PL, Guthrie CJ, Trattnig S, Robinson SD. Fast, high resolution QSM of the brainstem at 7T using super-resolution 2D EPI. In: Submitted to: Proc ISMRM Annual Meeting. 2019.

92. Betts J, Young K, Wise J. The Central Nervous System. In: Anatomy and Physiology [Internet]. Houston, TX, USA: OpenStax; [cited 2020 Feb 13]. Available from: openstax.org/books/anatomy-and-physiology/

93. Schäfer A, Forstmann BU, Neumann J, Wharton S, Mietke A, Bowtell R, Turner R. Direct visualization of the subthalamic nucleus and its iron distribution using high-resolution susceptibility mapping. Hum Brain Mapp. 2012 Dec;33(12):2831–42.

94. Okun MS. Deep-brain stimulation for Parkinson's disease. N Engl J Med. 2012 Oct 18;367(16):1529–38.

95. Perlmutter JS, Mink JW. Deep brain stimulation. Annu Rev Neurosci. 2006;29:229–57.

96. Patel NK, Khan S, Gill SS. Comparison of atlas- and magnetic-resonance-imaging-based stereotactic targeting of the subthalamic nucleus in the surgical treatment of Parkinson's disease. Stereotact Funct Neurosurg. 2008;86(3):153–61.

97. Wodarg F, Herzog J, Reese R, Falk D, Pinsker MO, Steigerwald F, Jansen O, Deuschl G, Mehdorn HM, Volksmann J. Stimulation site within the MRI-defined STN predicts postoperative motor outcome. Mov Disord Off J Mov Disord Soc. 2012 Jun;27(7):874–9.

98. Du G, Liu T, Lewis MM, Kong L, Wang Y, Connor J, Mailman RB, Huang X. Quantitative susceptibility mapping of the midbrain in Parkinson's disease. Mov Disord Off J Mov Disord Soc. 2016 Mar;31(3):317–24.

99. Ide S, Kakeda S, Ueda I, Watanabe K, Murakami Y, Moriya J, Ogasawara A, Futatsuya K, Sato T, Ohnari N, Okada K, Matsuyama A, Fujiwara H, Hisaoka M, Tsuji S, Liu T, Wang Y, Korogi Y. Internal structures of the globus pallidus in patients with Parkinson's disease: evaluation with quantitative susceptibility mapping (QSM). Eur Radiol. 2015 Mar;25(3):710–8.

100. Sclocco R, Beissner F, Bianciardi M, Polimeni JR, Napadow V. Challenges and opportunities for brainstem neuroimaging with ultrahigh field MRI. NeuroImage. 2018;168:412–26.

101. Robinson SD. Siemens DICOM Sort and Convert to NIfTI. MATLAB Central File Exchange. Available from: https://www.mathworks.com/matlabcentral/fileexchange/22508-siemens-dicom-sort-and-convert-to-nifti. 2008, updated 2020.

102. MATLAB. Natick, MA, USA: The Math Works Inc.; https://www.mathworks.com/products/matlab.html.

103. Liu C, Wei H, Li W. STI Suite [Internet]. University of California, Berkeley; Available from: people.eecs.berkeley.edu/~chunlei.liu/software.html

104. Wang Y. Morphology Enables Dipole Inversion (MEDI) Toolbox [Internet]. Cornell MRI Research Lab; Available from: http://pre.weill.cornell.edu/mri/pages/qsm.html

105. Chan K, Marques JP. SEPIA - SuscEptibility mapping PIpeline tool for phAse images. In: Proc ISMRM Annual Meeting. Montreal, Canada; 2019.

106. Dymerska B, Eckstein K. ROMEO Phase Unwrapping Algorithm (under development in-house). 2020.

107. Wei H, Zhang Y, Gibbs E, Chen N-K, Wang N, Liu C. Joint 2D and 3D phase processing for quantitative susceptibility mapping: application to 2D echo-planar imaging. NMR Biomed. 2017 Apr;30(4).

108. Rorden C. MRIcro [Internet]. University of South Carolina Neuropsychology Lab; Available from: https://people.cas.sc.edu/rorden/mricro/mricro.html

109. Straub S, Knowles BR, Flassbeck S, Steiger R, Ladd ME, Gizewski ER. Mapping the human brainstem: Brain nuclei and fiber tracts at 3 T and 7 T. NMR Biomed. 2019;32(9):e4118.

110. Goubran M, Rudko DA, Santyr B, Gati J, Szekeres T, Peters TM, Khan AR. In vivo normative atlas of the hippocampal subfields using multi-echo susceptibility imaging at 7 Tesla. Hum Brain Mapp. 2014 Aug;35(8):3588–601.

111. Stäb D, Bollmann S, Langkammer C, Bredies K, Barth M. Accelerated mapping of magnetic susceptibility using 3D planes-on-a-paddlewheel (POP) EPI at ultra-high field strength. NMR Biomed. 2017 Apr;30(4).

112. Jenkinson M, Pechaud M, Smith S. BET2: MR-based estimation of brain, skull and scalp surfaces. In: Proc of 11th Annual Meeting of the Organization for Human Brain Mapping. 2005.

113. Bachratá B. Quantitative Susceptibility Mapping using Echo Planar Imaging (Master Thesis). [Vienna, Austria]: Medical University of Vienna; 2017.

114. Schweser F, Robinson SD, de Rochefort L, Li W, Bredies K. An illustrated comparison of processing methods for phase MRI and QSM: removal of background field contributions from sources outside the region of interest. NMR Biomed. 2017 Apr;30(4).

115. Bollmann S, Rasmussen KGB, Kristensen M, Blendal RG, Østergaard LR, Plocharski M, O'Brien K, Langkammer C, Janke A, Barth M. DeepQSM - using deep learning to solve the dipole inversion for quantitative susceptibility mapping. NeuroImage. 2019 15;195:373–83.

116. Jung W, Yoon J, Ji S, Choi JY, Kim JM, Nam Y, Kim EY, Lee J. Exploring linearity of deep neural network trained QSM: QSMnet. NeuroImage. 2020 May 1;211:116619.

117. Zwanenburg JJM, Versluis MJ, Luijten PR, Petridou N. Fast high resolution whole brain T2* weighted imaging using echo planar imaging at 7T. NeuroImage. 2011 Jun 15;56(4):1902–7.

118. Jenkinson M. Improving the registration of B0-distorted EPI images using calculated cost function weights. In: Proc of 10th International Conference on Function Mapping of the Human Brain. 2004.

119. Jenkinson M, Bannister P, Brady M, Smith S. Improved optimization for the robust and accurate linear registration and motion correction of brain images. NeuroImage. 2002 Oct;17(2):825–41.